

NUMERICAL ENTROPY PRODUCTION FOR CENTRAL SCHEMES*

GABRIELLA PUPPO†

Abstract. In this work a detailed study of the numerical entropy production for both low- and high-order central schemes is carried out. Our data show that entropy production can be used to signal the presence of shocks. Moreover, once shocked cells have been identified, the spurious entropy production occurring in the remaining cells mimics the behavior of the local error, and therefore it can be used as an a posteriori error indicator. Applications to shock tracking and scheme adaptivity are given. We also investigate numerically the entropic properties of third and fourth order Central WENO schemes. To our knowledge, this is the first study of the entropic behavior of such high-order schemes.

Key words. conservation laws, numerical entropy, central difference schemes, high-order accuracy, a posteriori error

AMS subject classifications. Primary, 65M50; Secondary, 65M06, 65M15

DOI. 10.1137/S1064827502386712

1. Introduction. The numerical integration of systems of conservation laws has achieved remarkable successes. Several robust and accurate schemes are available, which provide well-resolved spurious-oscillations free numerical solutions. We mention high-order ENO [11], [25] and WENO [12] schemes (see [26] for a review), the Runge–Kutta discontinuous Galerkin (RKDG) scheme (see [7] and references therein), and high-order central schemes [22], [20], [17], [24].

As the order of the schemes increases, each time step becomes more and more costly computationally. Moreover, a straightforward componentwise application of nonoscillatory schemes for scalar equations can lead to oscillatory numerical solutions of systems of equations. An effective cure is to apply the scalar scheme along characteristic directions [24]. However, this results in a heavy computational overhead.

While numerical schemes become more and more sophisticated and expensive, a parallel field of research develops, focused on adaptive methods designed to use expensive schemes only where they are actually needed and effective.

Adaptive schemes follow very different strategies. The most common approach is to save computational effort through grid adaptivity. In this strategy, an error indicator must be provided whose purpose is to extract information from the numerical solution on the need to locally refine or coarsen the mesh. In this fashion, a fine grid is used only in those regions where the solution is rich in structure, and a coarse grid is turned to where the solution requires less detail.

A classical error indicator is based on the use of Richardson extrapolation; see [2] and [3] for its implementation in the CLAWPACK package. The main disadvantage of this approach is that Richardson extrapolation relies on local smoothness and can therefore be unreliable on nonsmooth solutions.

Another approach is based on the solution of an error equation which consists in an adjoint problem to the system of equations. This idea is investigated and tested

*Received by the editors January 21, 2002; accepted for publication (in revised form) May 11, 2003; published electronically December 19, 2003. This work was partially supported under MURST COFIN '99 and COFIN '01, coord. F. Brezzi, and GNCS-INDAM project *Numerical methods for hyperbolic and kinetic equations*.

<http://www.siam.org/journals/sisc/25-4/38671.html>

†Dipartimento di Matematica, Politecnico di Torino, Corso Duca degli Abruzzi 24, 10129 Torino, Italy (puppo@calvino.polito.it, <http://calvino.polito.it/~puppo>).

in [27], tailored to a particular finite volume scheme. We also quote the rigorous construction of error estimates for upwind finite volume schemes in [15] and staggered central schemes [18]. These approaches are backed by rigorous estimates, but they depend strongly on the particular scheme (first or at most second order accurate) being used. A review of duality arguments and the rigorous approach to a posteriori error analysis can be found in [6].

Recently, Karni and Kurganov [13] proposed an a posteriori error estimator, based on the approximate evaluation of the Lip' norm of the local residual. This indicator applies, in principle, to schemes of any order of accuracy. However, for third order schemes, the estimate of the error is based on a stencil which involves three time levels, and, when the order of accuracy of the scheme is increased further, even more time levels are involved. In [14] several numerical results are presented for schemes of order 2 to 3. Moreover, besides grid adaptivity, a different application of a posteriori error estimation is proposed. The idea is to use scheme adaptivity. Specifically, a simple linear scheme is used, except in those cells where the error indicator signals that a nonlinear nonoscillatory scheme is needed. The error indicator in [13] in fact works also as a smoothness indicator.

Finally, we mention [1], where an error indicator for steady Euler flows is proposed, which relies on the discrepancies of an entropy variable.

The results of this work indicate that a new error indicator can be constructed for unsteady flows as well based on the local numerical production of entropy. Moreover, this error indicator can be applied to a wide class of numerical schemes, without restrictions on the order of accuracy. In particular, we show results for schemes ranging from first to fourth order accurate. Furthermore, we will see that the evaluation of the numerical production of entropy allows us to classify transitions and single out shocks in the numerical solution. This will appear clearly in scalar as well as in gas dynamics examples.

There are no results at present on the entropic properties of higher than second order schemes. The data gathered from numerical tests, in this context, can suggest the entropic behavior of these schemes and give a direction for rigorous analysis. A result of this work is the conjecture that high-order central schemes may be essentially entropic, in the sense that spurious positive overshoots in the entropy production are possible, but their amplitude converges to zero, as the grid is refined.

The paper is organized as follows. In section 2 we define and compare the entropy productions for the Godunov and staggered Lax–Friedrichs schemes. For the linear advection equation, the form of the local truncation error is known, and we can compare the information obtained from the numerical entropy production with the expected error. In the following section, we compare the exact entropy production on a shock with the results obtained with the Godunov and Lax–Friedrichs schemes.

In section 3, we introduce the numerical entropy production for the second order Nessyahu–Tadmor scheme [22], for the Compact-C-WENO third order scheme [21] and for the fourth order Central WENO scheme [20], and we prove that, for a smooth flow, entropy production converges to zero with the same rate of local truncation error. Next, we compare the results obtained using these schemes on a few test cases.

In section 4 we propose a few applications of the study of numerical entropy production. First we use the data gathered from all schemes studied to address the issue of the behavior of numerical entropy production as a discontinuity detector. We illustrate the effectiveness of this procedure in tracking shocks in two test problems with wave interactions. Next, we study the possibility of using entropy production as a

local error indicator. Finally, we use entropy production as an indicator in an adaptive strategy designed to enhance the resolution of nonoscillatory schemes, following the approach proposed in [14].

We show our results on two simple scalar test problems and on Riemann problems from gas dynamics. This allows to thoroughly investigate the behavior of the entropy production on several schemes.

In the remaining part of this section, we introduce the main topic of this work.

We consider the scalar conservation law

$$(1.1) \quad u_t + f_x(u) = 0.$$

We choose an entropy function $\eta(u)$, and we associate to the conservation law the entropy inequality

$$(1.2) \quad \eta_t + \psi_x(u) \leq 0, \quad \text{with} \quad \psi'(u) = \eta'(u)f'(u).$$

We cover the computational region with control volumes $V_j^n = I_j \times [t^n, t^{n+1}]$, where $t^{n+1} = t^n + \Delta t$, $I_j = [x_j - h/2, x_j + h/2]$ and $x_{j+1} = x_j + h$.

Integrating the conservation law (1.1) over the control volumes V_j^n , we find the finite volume formulation:

$$(1.3) \quad \frac{1}{h} \int_{I_j} u^{n+1}(x) dx = \frac{1}{h} \int_{I_j} u^n(x) dx - \lambda \frac{1}{\Delta t} \int_{t^n}^{t^{n+1}} [f(u(I_j^+, \tau)) - f(u(I_j^-, \tau))] d\tau.$$

Here I_j^+ and I_j^- denote the right and left end points of the interval I_j and $u^n(x) = u(x, t^n)$, with $t^n = n\Delta t$. Finally, $\lambda = \Delta t/h$ is the mesh ratio.

Integrating the entropy inequality over the same control volume, we find the finite volume formulation of the entropy inequality:

$$(1.4) \quad \frac{1}{h} \int_{I_j} \eta(u^{n+1}(x)) dx - \frac{1}{h} \int_{I_j} \eta(u^n(x)) dx + \frac{\lambda}{\Delta t} \int_{t^n}^{t^{n+1}} [\psi(u(I_j^+, \tau)) - \psi(u(I_j^-, \tau))] d\tau \leq 0;$$

If the solution is smooth, it is well known that both (1.3) and (1.4) are equalities. If a shock crosses the V_j^n control volume, (1.3) is satisfied, but (1.4) will not be zero; instead its sign characterizes the physically relevant unique solution to (1.1).

When the finite volume formulation (1.3) is discretized, the corresponding discretized version of (1.4) will not be zero even for smooth flows. We claim that the amount by which (1.4) fails to be zero on smooth flows yields a measure of the local error.

More precisely, let $u_h(x, t)$ be the approximate solution to (1.3) found with a numerical scheme, with $u_h^n(x) = u_h(x, t^n)$. The present work is concerned with a numerical study of the quantity

$$(1.5) \quad S_j^n = \frac{1}{\Delta t} \left\{ \frac{1}{h} \int_{I_j} \eta(u_h^{n+1}(x)) dx - \frac{1}{h} \int_{I_j} \eta(u_h^n(x)) dx + \frac{\lambda}{\Delta t} \int_{t^n}^{t^{n+1}} [\psi(u_h)|_{I_j^+} - \psi(u_h)|_{I_j^-}] d\tau \right\},$$

which is the density of numerical entropy production in the V_j^n control volume (in the following it will be called local entropy production). The total entropy production of

the scheme then is

$$S = \sum_j \sum_n S_j^n h \Delta t.$$

It is interesting to note that (1.5) contains the same expression for the entropy used in [5] to construct a MUSCL method specifically designed to satisfy all entropy inequalities.

As we will see, central schemes based on staggered grids yield a natural way to evaluate S_j^n . Our tests suggest that the knowledge of S_j^n gives valuable information on the regularity of the solution and on the local error. Moreover the sign of S_j^n will give an indication of the entropic properties of the scheme.

2. Numerical entropy production for Lax–Friedrichs and Godunov schemes. For the Godunov scheme we discretize (1.3) on the control volumes $V_j^n = [x_j - \frac{h}{2}, x_j + \frac{h}{2}] \times [t^n, t^{n+1}]$. The cell averages $\{\bar{u}_j^n\}$ obtained from the previous time step are used to reconstruct the solution at the time level t^n as a piecewise constant function,

$$u^n(x) = \sum_j \bar{u}_j^n \chi_{I_j}(x),$$

where χ_{I_j} is the characteristic function of the interval $I_j = [x_j - \frac{h}{2}, x_j + \frac{h}{2}]$, and \bar{u}_j^n denotes the cell average at time t^n :

$$\bar{u}_j^n = \frac{1}{h} \int_{I_j} u^n(x) dx.$$

The updated cell-averages are given by

$$(2.1) \quad \bar{u}_j^{n+1} = \bar{u}_j^n - \lambda \left[f(u_{j+1/2}^*) - f(u_{j-1/2}^*) \right],$$

where $u_{j+1/2}^* = u^*(\bar{u}_j^n, \bar{u}_{j+1}^n)$ denotes the solution at $x_{j+1/2}$ of the Riemann problem with initial data $\{\bar{u}_j^n, \bar{u}_{j+1}^n\}$ centered at the cell interface $x = x_{j+1/2} = x_j + h/2$ (for the notation, see [19]).

Whenever the function u^* is well defined, i.e., when there are no stationary shocks, the Godunov scheme (2.1) yields a natural discretization of the cell entropy inequality (1.4). Since the numerical solution is piecewise constant, $u^n(x)|_{I_j} \equiv \bar{u}_j^n$. Moreover u^* is constant in time during the whole time step. Therefore the integrals in (1.4) can be evaluated exactly. We thus obtain the local entropy production for the Godunov scheme:

$$(2.2) \quad S_j^G = \frac{1}{\Delta t} \left\{ \eta(\bar{u}_j^{n+1}) - \eta(\bar{u}_j^n) + \lambda \left[\psi(u_{j+1/2}^*) - \psi(u_{j-1/2}^*) \right] \right\},$$

where from now on we will drop the index n from the left-hand side. Note that the numerical entropy flux $\Psi_{j+1/2} = \psi(u_{j+1/2}^*)$ is consistent with the exact entropy flux.

We now consider the staggered Lax–Friedrichs scheme. Again the solution at time t^n is reconstructed as a piecewise constant function,

$$u^n(x) = \sum_j \bar{u}_j^n \chi_{I_j}(x),$$

but now we integrate on the staggered control volumes $V_{j+1/2}^n = [x_j, x_{j+1}] \times [t^n, t^{n+1}]$. Therefore (see [28])

$$\bar{u}_{j+1/2}^{n+1} = \frac{1}{2}(\bar{u}_j^n + \bar{u}_{j+1}^n) - \frac{1}{h} \int_{t^n}^{t^{n+1}} [f(u(x_{j+1}, \tau)) - f(u(x_j, \tau))] d\tau.$$

The solution remains smooth at x_j and x_{j+1} , provided that $\lambda \leq \frac{1}{2} / \max |f'(u)|$. In this case, the integrals of the fluxes can be evaluated with quadrature. Using a first order quadrature formula, we obtain the staggered Lax–Friedrichs scheme:

$$(2.3) \quad \bar{u}_{j+1/2}^{n+1} = \frac{1}{2}(\bar{u}_j^n + \bar{u}_{j+1}^n) - \lambda [f(\bar{u}_{j+1}^n) - f(\bar{u}_j^n)].$$

The same discretization applied to the cell entropy inequality (1.4) yields the local entropy production for the staggered Lax–Friedrichs scheme:

$$(2.4) \quad S_{j+1/2}^{LF} = \frac{1}{\Delta t} \left\{ \eta(\bar{u}_{j+1/2}^{n+1}) - \frac{1}{2} [\eta(\bar{u}_{j+1}^n) + \eta(\bar{u}_j^n)] + \lambda [\psi(\bar{u}_{j+1}^n) - \psi(\bar{u}_j^n)] \right\}.$$

2.1. Computing the entropy production for the linear advection equation. The scalar conservation law (1.1) admits an infinite number of entropy functions (in fact any convex function is an admissible entropy; see, for instance, [10]). Instead of studying all resulting entropy inequalities, it is enough to consider only the family of Kruzkov's entropy functions [16], which are given by

$$\eta(u; c) = |u - c| \quad \text{with} \quad \psi(u; c) = \text{sgn}(u - c)(f(u) - f(c)) \quad \forall c \in \mathcal{R}.$$

However, Kruzkov's entropies are not practical for the present application, because S_j is automatically zero in many nontrivial cases, unless c is chosen as a function of the local solution. Thus it would be necessary to change c in each cell. Take for example the Godunov scheme. From (2.2), the local entropy production computed using Kruzkov's entropy is

$$S_j^G(c) = \frac{1}{\Delta t} \left\{ |\bar{u}_j^{n+1} - c| - |\bar{u}_j^n - c| + \lambda \left[\text{sgn}(u_{j+1/2}^* - c)(f(u_{j+1/2}^*) - f(c)) - \text{sgn}(u_{j-1/2}^* - c)(f(u_{j-1/2}^*) - f(c)) \right] \right\}.$$

Suppose $f'(u) > 0$ and $\bar{u}_{j-1}^n > \bar{u}_j^n$. Then $u_{j+1/2}^* = \bar{u}_j^n$ and $u_{j-1/2}^* = \bar{u}_{j-1}^n$. Moreover, if CFL holds, $\bar{u}_{j-1}^n \geq \bar{u}_j^{n+1} \geq \bar{u}_j^n$. Suppose $c \notin [\bar{u}_j^n, \bar{u}_{j-1}^n]$; then

$$\text{sgn}(\bar{u}_j^{n+1} - c) = \text{sgn}(\bar{u}_j^n - c) = \text{sgn}(u_{j+1/2}^* - c) = \text{sgn}(u_{j-1/2}^* - c).$$

If we substitute this into the equation for $S_j^G(c)$, together with the expression for \bar{u}_j^{n+1} , given by (2.1), we immediately find $S_j^G(c) = 0$. To find a nonzero value for $S_j^G(c)$, we must take $c \in [\bar{u}_j^n, \bar{u}_{j-1}^n]$; i.e., it is necessary to change c in each cell. It is easy to see that the same behavior will occur whenever c does not belong to the range of the values of \bar{u}^n which are involved in the construction of \bar{u}_j^{n+1} for all schemes studied in this work.

In the following discussion and in all the numerical tests for the scalar equation, we will therefore consider the entropy $\eta(u) = u^2$, which does not yield $S_j \equiv 0$. This

choice appears quite often in the literature: the entropy inequality is proven for the particular case $\eta(u) = \frac{1}{2}u^2$ for the schemes in, among others, [22], [8].

We wish to compare the densities of entropy production obtained with the Godunov and the staggered Lax–Friedrichs schemes. We consider the linear advection equation $u_t + u_x = 0$. In this case, $u^*(u_j, u_{j+1}) = u_j$. The entropy production for the Godunov scheme (2.2) for the entropy $\eta(u) = u^2$ becomes

$$S_j^G = \frac{1}{\Delta t} \{ (\bar{u}_j^{n+1})^2 - (\bar{u}_j^n)^2 + \lambda [(\bar{u}_j^n)^2 - (\bar{u}_{j-1}^n)^2] \}.$$

Substituting the expression for \bar{u}_j^{n+1} from (2.1), we find that

$$(2.5) \quad S_j^G = -h(1-\lambda) \left(\frac{\bar{u}_j^n - \bar{u}_{j-1}^n}{h} \right)^2.$$

In the linear advection case, it is possible to motivate the choice $\eta(u) = u^2$ with the following argument (Denise Aregba Driollet, private communication).

Consider Kruzkov's entropies for the particular case of the linear advection equation $u_t + u_x = 0$:

$$\eta(u; c) = |u - c| \quad \psi(u; c) = \operatorname{sgn}(u - c)(u - c) = |u - c|.$$

For the Godunov scheme, we obtain the local entropy production:

$$S_{j;c}^G = \frac{1}{\Delta t} \{ |\bar{u}_j^{n+1} - c| - |\bar{u}_j^n - c| + \lambda(|\bar{u}_j^n - c| - |\bar{u}_{j-1}^n - c|) \}.$$

Suppose, without loss of generality, that $\bar{u}_j^n \geq \bar{u}_{j-1}^n$. Then $\bar{u}_{j-1}^n \leq \bar{u}_j^{n+1} \leq \bar{u}_j^n$, if CFL holds, and the following four cases are possible:

- 1) $c \leq \bar{u}_{j-1}^n, \quad S_{j;c}^G = 0,$
- 2) $\bar{u}_{j-1}^n \leq c \leq \bar{u}_j^{n+1}, \quad S_{j;c}^G = \frac{2\lambda}{\Delta t}(\bar{u}_{j-1}^n - c),$
- 3) $\bar{u}_j^{n+1} \leq c \leq \bar{u}_j^n, \quad S_{j;c}^G = \frac{2}{\Delta t}(1-\lambda)(c - \bar{u}_j^n),$
- 4) $c \geq \bar{u}_j^n, \quad S_{j;c}^G = 0.$

Now let us compute the sum of all Kruzkov's local entropy productions (we suppress the index n):

$$\begin{aligned} \langle S_{j;c}^G \rangle &= \int_{-\infty}^{+\infty} S_{j;c}^G \, dc = \int_{\bar{u}_{j-1}^n}^{\bar{u}_j^n - \lambda(\bar{u}_j^n - \bar{u}_{j-1}^n)} \frac{2\lambda}{\Delta t}(\bar{u}_{j-1}^n - c) \\ &\quad + \int_{\bar{u}_j^n - \lambda(\bar{u}_j^n - \bar{u}_{j-1}^n)}^{\bar{u}_j^n} \frac{2}{\Delta t}(1-\lambda)(c - \bar{u}_j^n) \\ &= -\frac{1}{\Delta t}\lambda(1-\lambda)(\bar{u}_j^n - \bar{u}_{j-1}^n)^2, \end{aligned}$$

which is exactly the expression for S_j^G , obtained before with $\eta(u) = u^2$. Therefore the choice $\eta(u) = u^2$ yields the integral of the local entropy production, over all Kruzkov's entropies.

We now compute the local entropy production for the staggered Lax–Friedrichs scheme, again for $\eta(u) = u^2$ on the linear advection equation. In order to compare

the two schemes, we consider $\Delta t_{LF} = \frac{1}{2}\Delta t$, since the CFL ratio for the staggered Lax–Friedrichs scheme is half the corresponding value of the Godunov scheme. The mesh width h is the same for the two schemes. We find that

$$S_{j-1/2}^{LF} = \frac{1}{\frac{\Delta t}{2}} \left\{ (\bar{u}_{j-1/2}^{n+1})^2 - \frac{1}{2} [(\bar{u}_j^n)^2 + (\bar{u}_{j-1}^n)^2] + \frac{\Delta t}{2h} [(\bar{u}_j^n)^2 - (\bar{u}_{j-1}^n)^2] \right\}.$$

Substituting $\bar{u}_{j-1/2}^{n+1}$ with the quantity given by the Lax–Friedrichs scheme (2.3), we find that

$$(2.6) \quad S_{j-1/2}^{LF} = -h(1-\lambda) \frac{1+\lambda}{2\lambda} \left(\frac{\bar{u}_j^n - \bar{u}_{j-1}^n}{h} \right)^2.$$

Note that in both cases the entropy is negative, provided CFL holds, i.e., $1-\lambda > 0$.

Remark. If we compute the entropy production for the Lax–Friedrichs scheme with Kruzkov’s entropies, we can follow the same steps already described for the Godunov scheme. In each control volume $V_{j-1/2}$ and for each value of c , we find a corresponding local entropy production $S_{j-1/2;c}^{LF}$. Again, if we compute the integral of $S_{j-1/2;c}^{LF}$ over all c , we easily find that $\langle S_{j-1/2;c}^{LF} \rangle = S_{j-1/2}^{LF}$, where $S_{j-1/2}^{LF}$ is given in (2.6). Therefore, in this case too, the entropy, $\eta(u) = u^2$, yields the integral of the local entropy production over all Kruzkov’s entropies.

We now wish to compare the expressions for S_j^G and $S_{j-1/2}^{LF}$ with the local truncation error of these schemes. To this end, we consider smooth flow and we compute the modified equations for the Godunov and Lax–Friedrichs schemes (see [19, chap. 11]).

For the Godunov scheme we find the following modified equation:

$$(2.7) \quad u_t + u_x = \frac{h}{2}(1-\lambda)u_{xx}.$$

Now we compute the modified equation for the Lax–Friedrichs scheme. To compare the two methods, we need to bring the numerical solution to the same time level; thus we apply the Lax–Friedrichs scheme twice, obtaining the method

$$\bar{u}_j^{n+2} = \bar{u}_j^n - \lambda(\bar{u}_{j+1}^n - \bar{u}_{j-1}^n) + \left(\frac{1}{4} + \lambda^2 \right) (\bar{u}_{j+1}^n - 2\bar{u}_j^n + \bar{u}_{j-1}^n).$$

The modified equation for this scheme is

$$(2.8) \quad u_t + u_x = \frac{h}{2}(1-\lambda) \frac{1+\lambda}{2\lambda} u_{xx}.$$

Note the similarities between the local entropy production and the leading term in the truncation error (appearing on the right-hand side of the modified equations).

2.2. Computing the entropy production on a shock. In this section, the entropy production on a shock separating two constant states is computed, comparing the exact result with the numerical entropy production due to Godunov and Lax–Friedrichs schemes.

We consider Burgers’ equation

$$u_t + \left(\frac{1}{2}u^2 \right)_x = 0$$

with the initial condition

$$u(x, 0) = \begin{cases} u_L, & x < x_0, \\ u_R, & x > x_0. \end{cases}$$

If $u_L > u_R$, the exact solution is a shock, traveling with speed $s = \frac{1}{2}(u_L + u_R)$. Suppose the shock is initially located at $x = x_0$ in the interval $I_{j+1/2} = [x_j, x_{j+1}]$, i.e., $x_j < x_0 < x_{j+1}$. Suppose moreover that the shock does not leave the control volume $V_{j+1/2} = I_{j+1/2} \times [0, \Delta t]$ in the time Δt .

The exact local entropy production in the cell containing the shock can be easily calculated. Let $S(u_L, u_R)$ be the exact entropy production due to a shock between the two states u_L and u_R , and again let $\eta = u^2$. Then

$$(2.9) \quad S(u_L, u_R) = -\frac{1}{6h}(u_L - u_R)^3,$$

where of course $S(u_L, u_R) < 0$ if $u_L > u_R$ (see also [19]).

Usually, numerical schemes spread a shock over more than one cell, creating at least one intermediate state u_C .

With the same technique, we can find the total entropy production resulting from this configuration with two shocks; namely,

$$\begin{aligned} S_C &= S(u_L, u_C) + S(u_C, u_R) \\ &= -\frac{1}{6h}(u_L - u_C)^3 - \frac{1}{6h}(u_C - u_R)^3. \end{aligned}$$

It can be easily shown that

$$|S(u_L, u_R)| > |S_C|,$$

provided that the profile is monotone, i.e., $u_L > u_C > u_R$. Therefore, the entropy production diminishes (in absolute value) as the profile is spread across the cells. Since the spurious intermediate states do not disappear as $h \rightarrow 0$, the numerical entropy production on a shock due to a particular scheme will not converge to the exact entropy production even as $h \rightarrow 0$. However, as we will see below this is not the only source of error in the numerical entropy dissipated on a shock.

Let us now compute the entropy production obtained with the Godunov and Lax-Friedrichs schemes on a shock separating the two states $u_L > u_R$.

Consider the initial data

$$u_i^n = \begin{cases} u_L, & i \leq j, \\ u_R, & i > j. \end{cases}$$

Suppose that $s > 0$. After one time step, there is only one cell where the entropy production is nonzero, namely, for $i = j + 1$. On this cell, for $\eta(u) = u^2$, we find that

$$\begin{aligned} S^G &= \frac{1}{\Delta t} \left\{ (\bar{u}_{j+1}^{n+1})^2 - (\bar{u}_{j+1}^n)^2 + \frac{2}{3}\lambda \left[(u_{j+3/2}^*)^3 - (u_{j+1/2}^*)^3 \right] \right\} \\ &= \frac{1}{\Delta t} \left\{ \left[u_R - \frac{\lambda}{2}(u_R^2 - u_L^2) \right]^2 - u_R^2 + \frac{2}{3}\lambda [u_R^3 - u_L^3] \right\}. \end{aligned}$$

We add and subtract the exact entropy production $S(u_L, u_R)$. After rearranging, we finally find that

$$(2.10) \quad S^G = S(u_L, u_R) - \frac{s}{h}(u_L - u_R)^2(1 - \lambda s).$$

Since $s > 0$ in this example, we can see that the Godunov scheme provides an extra entropy dissipation with respect to the exact solution if CFL is satisfied.

Consider now the entropy production for the staggered Lax–Friedrichs scheme. Here we find a nonzero entropy production only in the cell centered at $x_{j+1/2}$:

$$S^{LF} = S(u_L, u_R) - \frac{1}{\Delta t_{LF}} (u_L - u_R)^2 \left[\frac{1}{4} - \frac{\lambda_{LF}^2}{4} (u_L + u_R)^2 \right],$$

where Δt_{LF} and λ_{LF} are the time step and mesh ratio for the Lax–Friedrichs scheme. Again, we have an extra amount of entropy production with respect to the exact solution.

To compare S^{LF} and S^G , we substitute, as in the previous section, $\lambda_{LF} = \frac{1}{2}\lambda$. This yields

$$(2.11) \quad \begin{aligned} S^G &= S(u_L, u_R) - hs \left(\frac{u_L - u_R}{h} \right)^2 (1 - \lambda s), \\ S^{LF} &= S(u_L, u_R) - hs \left(\frac{u_L - u_R}{h} \right)^2 (1 - \lambda s) \frac{1 + \lambda s}{2\lambda s}. \end{aligned}$$

In both cases, the numerical entropy production does not converge to $S(u_L, u_R)$ as $h \rightarrow 0$. The situation will be further complicated in the following time steps, when the shock will be spread on a few cells. Therefore we have two competing phenomena on a shock: on the one hand the numerical scheme tends to dissipate more entropy on a given shock than the exact solution; on the other hand, the creation of intermediate states tends to diminish the amount of entropy dissipated on the shock. However, in the cells containing shocks we are not interested in evaluating the local error, which does not go to zero. We are mainly interested in knowing where the shock occurs. The entropy production contains this information, because, for both schemes, as in the exact case, $S \simeq \frac{1}{h}$ in shocked cells. In section 3.2, it will be shown that the same estimate holds for higher-order schemes. The numerical tests will show that this behavior persists in the following time steps and for higher-order schemes, even in the case of systems of equations.

Finally we wish to stress the similarity with the linear case. In fact, for linear advection, $S(u_L, u_R) = 0$, and, in the case $u_t + u_x = 0$ studied in the previous section, $s = 1$. Therefore we obtain the same expressions we have found in (2.5) and (2.6).

2.3. Numerical results. We test the schemes on two simple problems. The tests were chosen in order to study the behavior of the entropy production on a smooth transition, a shock, a contact discontinuity, and a transition with a jump in the first derivative, as an example of a nonsmooth solution. The two test problems considered are described below.

Test #1. Burger equation:

$$\begin{aligned} u_t + \left(\frac{1}{2}u^2\right)_x &= 0 \quad \text{on } (-1, 1), \\ u(x, t = 0) &= 1 + \frac{1}{2}\sin(\pi x) \end{aligned}$$

with periodic boundary conditions.

This IVP develops a shock at $T_s = 2/\pi$. The numerical solution is sampled at $T = 0.5 < T_s$ to illustrate the results on a nonlinear smooth flow. At $T = 1.5$ this test shows the behavior of the entropy production after shock formation.

Test #2. Linear advection:

$$\begin{aligned} u_t + u_x &= 0 \quad \text{on } (-1, 1), \\ u(x, t = 0) &= \begin{cases} \cos(\frac{\pi}{2}x), & -1 \leq x \leq 0, \\ \sin(\pi x), & 0 < x \leq 1, \end{cases} \end{aligned}$$

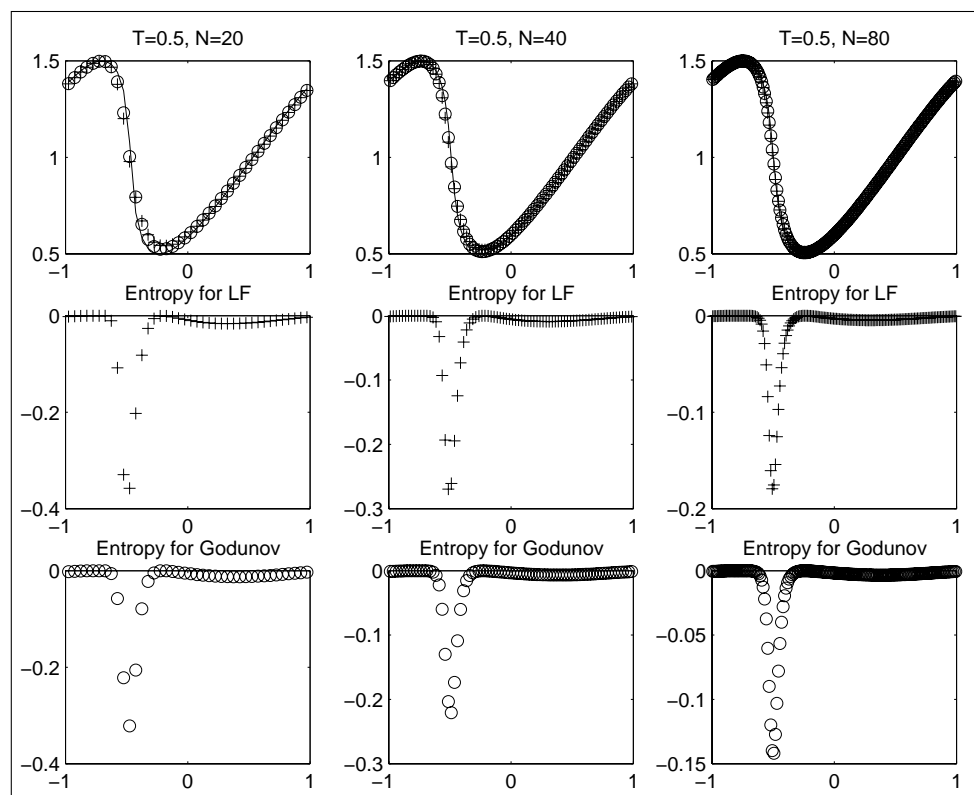


FIG. 1. Burgers' equation. Solution at $T = 0.5$. Comparison between the entropy production of Lax-Friedrichs (+) and Godunov (o) schemes on a smooth flow. Godunov has $\lambda = 0.66$, while Lax-Friedrichs has $\lambda = 0.33$.

with periodic boundary conditions.

The initial data contain a discontinuity and an angular point, induced by the boundary conditions. Therefore this test describes the behavior of the entropy indicator on a contact wave and on a region of nonsmooth flow.

The results for Test #1 appear in Figure 1 for the case $T = 0.5$ and in Figure 2 for $T = 1.5$. The first row of Figure 1 shows the two numerical solutions superposed. Each column corresponds to a grid size. Here N is the number of grid points per unit length. In the second and third rows we find the local entropy production for the two schemes.

The two numerical solutions are almost indistinguishable. It is apparent that entropy production approximately halves as the number of grid points is doubled. Moreover, as expected, the staggered Lax-Friedrichs scheme is slightly more diffusive than the Godunov scheme, and in fact the entropy production is slightly larger for the Lax-Friedrichs scheme.

Figure 2 shows the results for Test #1 after shock formation. Here we note that for both schemes the entropy production on the shock approximately doubles as the grid is refined, as expected from the analysis in section 2.2. This behavior is markedly different from the one we noticed for smooth flows, and it permits us to single out shocks from the rest of the flow.

In Figure 3 we show the results obtained on the contact discontinuity of Test #2

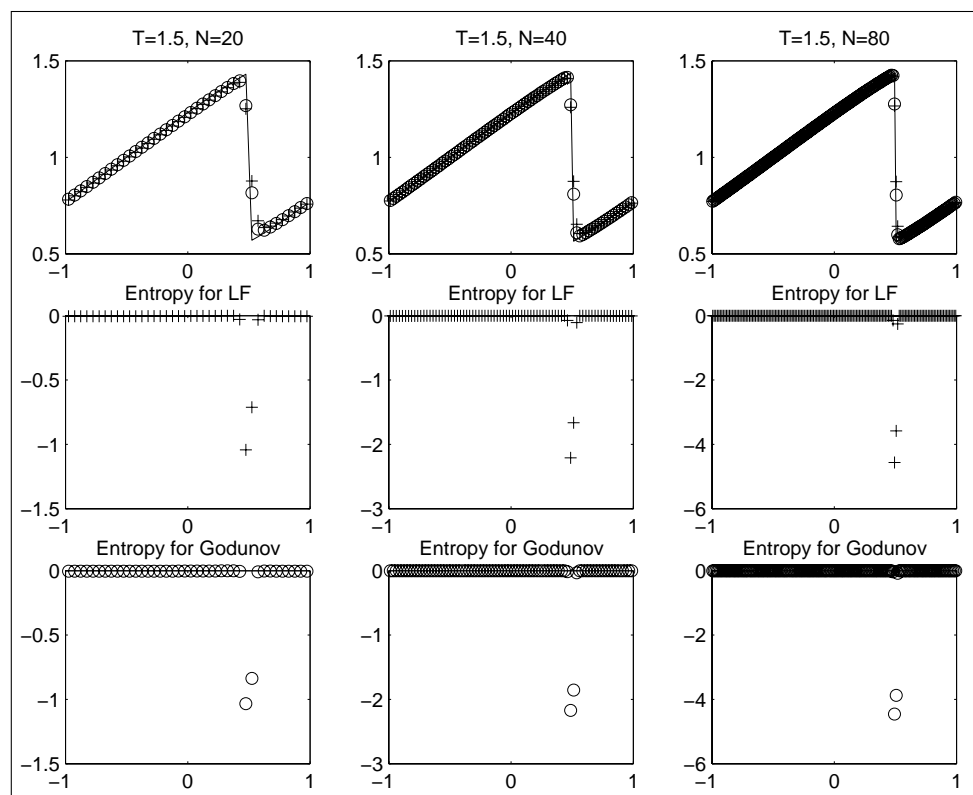


FIG. 2. Burgers' equation. Solution at $T = 1.5$. Comparison between the entropy production of Lax-Friedrichs (+) and Godunov (o) schemes on a shock. Godunov has $\lambda = 0.66$, while Lax-Friedrichs has $\lambda = 0.33$.

for several grid sizes. As the grid is fine enough to resolve it, the contact wave is characterized by a peak in the entropy production. The amplitude of this spurious peak grows slowly under grid refinement (see also Table 4). From the data in Table 4 for both first order schemes, we see that $S_j \simeq h^{-1/5}$, since on the contact discontinuity the peak in the entropy production approximately doubles after five grid refinements. However, this behavior is found only for first order schemes in the scalar case. For systems of equations, the entropy production on contacts seems to be approximately constant under grid refinement for all schemes tested in this work (see Figure 8).

The amplitude of the peak of spurious entropy production on the angular point goes to zero with an order comparable to h .

3. Numerical entropy production for high-order schemes. In this section we define the local entropy production for some high-order central schemes (see [28] for a review on central schemes). In particular, we will consider the second order Nessyahu-Tadmor scheme [22] (NT), the third order Compact Central WENO scheme (CW3) [21], and the fourth order Central WENO scheme (CW4) [20]. In the following subsections we first review the structure of central schemes and define the entropy production for these schemes; next we show that the entropy production is of the same order, with respect to Δt , of local truncation error on smooth flows. Finally, we study the behavior of entropy production for the NT, CW3, and CW4 schemes.

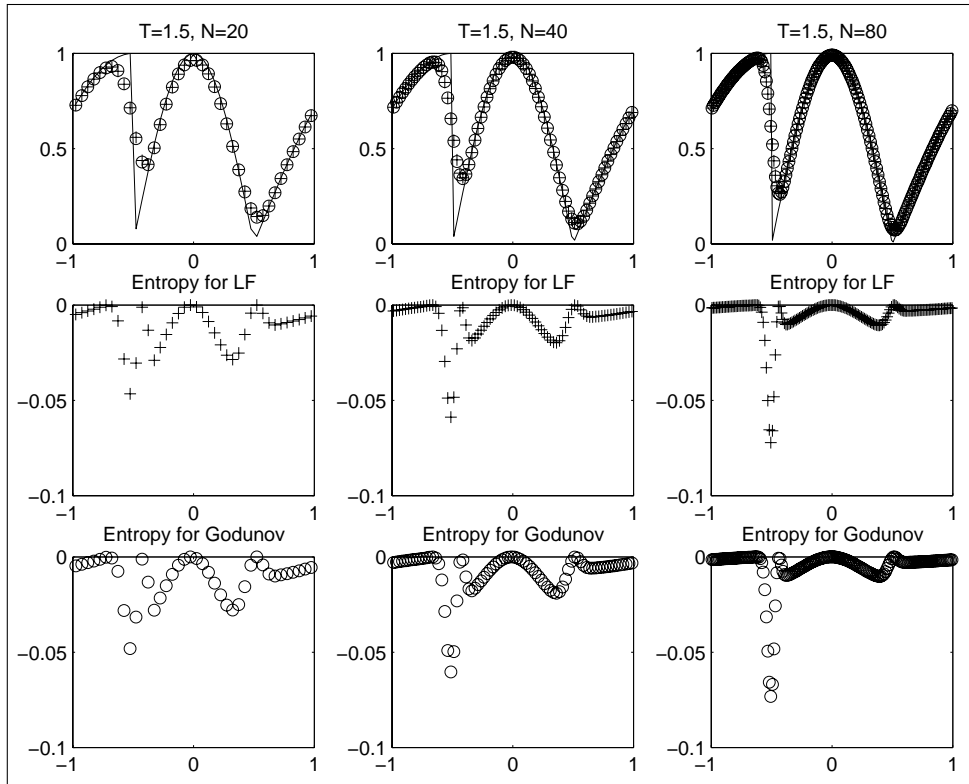


FIG. 3. Linear advection. Solution at $T = 1.5$. Comparison between the entropy production of Lax-Friedrichs (+) and Godunov (o) schemes on a contact wave. Godunov has $\lambda = 0.9$, while Lax-Friedrichs has $\lambda = 0.45$.

3.1. Entropy production for central schemes. All schemes in this section are based on a piecewise polynomial reconstruction of degree d :

$$u^n(x) = \sum_j R_j^d(x) \chi_{I_j}(x),$$

where all polynomials R_j^d are obtained from the cell averages at time t^n .

As in the staggered Lax-Friedrichs scheme, the equation is integrated on the staggered control volume $V_{j+1/2}^n$, and the finite volume formulation for these schemes becomes

$$(3.1) \quad \bar{u}_{j+1/2}^{n+1} = \frac{1}{h} \int_{x_j}^{x_{j+1}} u^n(x) dx - \frac{1}{h} \int_{t^n}^{t^{n+1}} [f(u(x_{j+1}, t)) - f(u(x_j, t))] dt,$$

where the staggered average of $u^n(x)$ (first term on the right-hand side) is computed using the reconstruction. The advantage of this approach is that the discontinuities in the initial data, located at the end points of the cells, $x_{j+1/2}$, now lie in the middle of the control volumes. Therefore the waves resulting from the interaction of the data $u^n(x_{j+1/2}^-)$ and $u^n(x_{j+1/2}^+)$ do not reach the boundaries of the control volume if Δt is small enough. More precisely, if Δt is chosen in order to satisfy the more restrictive

CFL condition

$$(3.2) \quad \Delta t \leq \frac{h}{2} \frac{1}{\max |f'(u)|},$$

then we can assume that the solution u remains smooth at x_j and x_{j+1} for $t^n \leq t \leq t^{n+1}$, and the time integrals in (3.1) can be computed with quadrature.

Let

$$\frac{1}{\Delta t} \int_{t^n}^{t^{n+1}} f(u(x_j, t)) dt \simeq \sum_{l=1}^M w_l f(u(x_j, t^n + \tau_l))$$

be a suitable quadrature rule for the time integrals of the fluxes. Now it is necessary to estimate u at the intermediate times $t^n + \tau_l$.

The Nessyahu–Tadmor scheme uses the midpoint rule to compute the time integrals. Thus $M = 1$, $\tau_1 = \Delta t/2$, and $u_j^{n+1/2} \simeq u(x_j, t^n + \Delta t/2)$ is estimated with Taylor expansion, using the equations $u_t|_j = -f_x(u)|_j$.

For the CW3 and CW4 schemes, Simpson's rule is used. In this case, $M = 2$ and three intermediate states must be computed:

$$u_j^n = u^n(x_j), \quad u_j^{n+1/2} \simeq u\left(x_j, t^n + \frac{\Delta t}{2}\right), \quad u_j^{n+1} \simeq u(x_j, t^n + \Delta t).$$

The first value is computed from the reconstruction. The remaining two quantities are obtained applying a Runge–Kutta scheme with natural continuous extension [31] to the equations $u_t|_j = -f_x(u)|_j$ (see [20]).

Define the local entropy production for these schemes as

$$(3.3) \quad S_{j+1/2} = \frac{1}{\Delta t} \left\{ \int_{x_j}^{x_{j+1}} \eta(u^{n+1}(x)) - \int_{x_j}^{x_{j+1}} \eta(u^n(x)) \right. \\ \left. + \lambda \sum_{l=1}^M w_l [\psi(u_j^{(l)}) - \psi(u_{j+1}^{(l)})] \right\},$$

where $u_j^{(l)}$ is the approximation computed by the scheme to $u(x_j, t^n + \tau_l)$, appearing in the quadrature rule for the fluxes.

Note that the quantities needed to compute $S_{j+1/2}$ (i.e., $u^n(x)$, $u^{n+1}(x)$, $u(x_j, t^n + \tau_l)$) must be computed in order to update the solution. Thus the entropy indicator does not require a heavy computational overhead.

3.2. Convergence rate. In this section we show that the local entropy production is

$$(3.4) \quad \begin{aligned} S_{j+1/2}^n &= O(\Delta t)^r && \text{on smooth flows,} \\ S_{j+1/2}^n &\leq O\left(\frac{1}{\Delta t}\right) && \text{on nonsmooth flows,} \end{aligned}$$

where r is the accuracy of the underlying scheme. To prove this statement, we use the same framework of the evaluation of the order of accuracy of a numerical scheme for a PDE. Namely, we will compute the entropy production resulting from the application of the scheme for a single time step.

Let $v(x, t)$ be the exact solution of problem (1.1), and let $u(x, t)$ be the numerical solution. Consider a generic time t^n . Apply the numerical scheme for a single time step, starting from the exact cell averages, i.e.,

$$\bar{u}_j^n = \bar{v}_j^n.$$

Then, if we are using an r th order accurate scheme, and the exact solution v is smooth,

$$(3.5) \quad \bar{u}_{j+1/2}^{n+1} = \bar{v}_{j+1/2}^{n+1} + O(\Delta t)^{r+1}.$$

We start, for simplicity, from the Nessyahu–Tadmor scheme.

DEFINITION 1. *The local entropy production of the Nessyahu–Tadmor scheme on the control volume $V_{j+1/2}^{n+1} = [x_j, x_{j+1}] \times [t^n, t^{n+1}]$ is given by*

$$(3.6) \quad S_{j+1/2}^{n+1} = \frac{1}{\Delta t} \left\{ \frac{1}{2} \eta(u^{n+1}(x_j + \frac{h}{4})) + \frac{1}{2} \eta(u^{n+1}(x_j + \frac{3}{4}h)) - \frac{1}{2} \eta(u^n(x_j + \frac{h}{4})) - \frac{1}{2} \eta(u^n(x_j + \frac{3}{4}h)) + \lambda [\psi(u_{j+1}^{n+1/2}) - \psi(u_j^{n+1/2})] \right\}.$$

The point values of u at $x_j + \frac{1}{4}h$ and $x_j + \frac{3}{4}h$ are computed through the reconstruction. Thus, it is necessary to evaluate the reconstruction at the end of each time step. The intermediate state $u_j^{n+1/2}$ is computed within the Nessyahu–Tadmor scheme to update the solution.

Other definitions for the entropy production are possible, as long as the quadrature rules in space and time are accurate enough.

PROPOSITION 1. *Suppose we are using the second order Nessyahu–Tadmor scheme for one time step with $\bar{u}_j^n = \bar{v}_j^n$. Consider a smooth entropy η and a smooth entropy flux ψ . Then the entropy production in the control volume $V_{j+1/2}^{n+1}$ satisfies the following estimates:*

$$(3.7) \quad \begin{aligned} S_{j+1/2}^{n+1} &= O(\Delta t)^2 \quad \text{on smooth flows,} \\ S_{j+1/2}^{n+1} &\leq O\left(\frac{1}{\Delta t}\right) \quad \text{on nonsmooth flows.} \end{aligned}$$

Proof. We are supposing the scheme is second order accurate; i.e., we are not in the presence of local extrema, where the Nessyahu–Tadmor scheme degenerates to first order. Thus either $u'_j = (\bar{u}_{j+1} - \bar{u}_j)/h$ or $u'_j = (\bar{u}_j - \bar{u}_{j-1})/h$. To fix ideas, consider the second case. Thus

$$(3.8) \quad \begin{aligned} u^{n+1}(x_j + \frac{1}{4}h) &= \bar{u}_{j+1/2}^{n+1} - \frac{h}{4}u'_{j+1/2} = \frac{3}{4}\bar{u}_{j+1/2}^{n+1} + \frac{1}{4}\bar{u}_{j-1/2}^{n+1}, \\ u^{n+1}(x_j + \frac{3}{4}h) &= \bar{u}_{j+1/2}^{n+1} + \frac{h}{4}u'_{j+1/2} = \frac{5}{4}\bar{u}_{j+1/2}^{n+1} - \frac{1}{4}\bar{u}_{j-1/2}^{n+1}, \\ u^n(x_j + \frac{1}{4}h) &= \bar{u}_j^n + \frac{h}{4}u'_j = \frac{5}{4}\bar{u}_j^n - \frac{1}{4}\bar{u}_{j-1}^n, \\ u^n(x_j + \frac{3}{4}h) &= \bar{u}_{j+1}^n - \frac{h}{4}u'_{j+1} = \frac{3}{4}\bar{u}_{j+1}^n + \frac{1}{4}\bar{u}_j^n, \end{aligned}$$

where the slopes at j and $j+1$ are computed at time t^n , while the staggered slopes at $j+1/2$ and $j-1/2$ are computed at time t^{n+1} . Consider the first equation. Substituting the exact solution,

$$\begin{aligned} u^{n+1}(x_j + \frac{1}{4}h) &= \frac{3}{4}\bar{v}_{j+1/2}^{n+1} + \frac{1}{4}\bar{v}_{j-1/2}^{n+1} + O(\Delta t)^3 \\ &= v^{n+1}(x_j + \frac{1}{4}h) + \frac{13}{4} \frac{h^2}{24} (v_{xx})_{j+1/4} + O(h)^3 + O(\Delta t)^3, \end{aligned}$$

where the shorthand $(v_{xx})_{j+1/4}^{n+1}$ denotes $(v_{xx})(x_j + \frac{1}{4}h, t^{n+1})$. A similar notation will also be used below. Using the smoothness of η and $\lambda h = \Delta t$, one finds that

$$(3.9) \quad \begin{aligned} \eta\left(u^{n+1}\left(x_j + \frac{1}{4}h\right)\right) &= \eta\left(v^{n+1}\left(x_j + \frac{1}{4}h\right)\right) + \frac{13}{4} \frac{h^2}{24} \eta'\left(v_{j+1/4}^{n+1}\right) (v_{xx})_{j+1/4}^{n+1} \\ &\quad + O(\Delta t)^3. \end{aligned}$$

Analogously,

$$\eta \left(u^{n+1} \left(x_j + \frac{3}{4}h \right) \right) = \eta \left(v^{n+1} \left(x_j + \frac{3}{4}h \right) \right) - \frac{11}{4} \frac{h^2}{24} \eta' \left(v_{j+3/4}^{n+1} \right) (v_{xx})_{j+3/4}^{n+1} + O(\Delta t)^3, \quad (3.10)$$

$$\eta \left(u^n \left(x_j + \frac{1}{4}h \right) \right) = \eta \left(v^n \left(x_j + \frac{1}{4}h \right) \right) - \frac{11}{4} \frac{h^2}{24} \eta' \left(v_{j+1/4}^n \right) (v_{xx})_{j+1/4}^n + O(\Delta t)^3, \quad (3.11)$$

$$\eta \left(u^n \left(x_j + \frac{3}{4}h \right) \right) = \eta \left(v^n \left(x_j + \frac{3}{4}h \right) \right) + \frac{13}{4} \frac{h^2}{24} \eta' \left(v_{j+3/4}^n \right) (v_{xx})_{j+3/4}^n + O(\Delta t)^3. \quad (3.12)$$

Adding (3.9) and (3.10) and subtracting (3.11) and (3.12), one finds the contribution to the entropy production of the terms involving η :

$$\begin{aligned} & \frac{1}{2} \eta(u_{j+1/4}^{n+1}) + \frac{1}{2} \eta(u_{j+3/4}^{n+1}) - \frac{1}{2} \eta(u_{j+1/4}^n) - \frac{1}{2} \eta(u_{j+3/4}^n) \\ &= \frac{1}{h} \int_{x_j}^{x_{j+1}} \eta(v^{n+1}(x)) \, dx - \frac{1}{4} \frac{h^2}{24} \eta_{xx}(\xi_1, t^{n+1}) + \frac{1}{4} \frac{h^2}{24} \eta'(v_{j+1/2}^{n+1}) (v_{xx})_{j+1/2}^{n+1} \\ & \quad - \frac{1}{h} \int_{x_j}^{x_{j+1}} \eta(v^n(x)) \, dx - \frac{1}{4} \frac{h^2}{24} \eta_{xx}(\xi_2, t^n) + \frac{1}{4} \frac{h^2}{24} \eta'(v_{j+1/2}^n) (v_{xx})_{j+1/2}^n + O(\Delta t)^3 \\ (3.13) \quad &= \frac{1}{h} \int_{t^n}^{t^{n+1}} \int_{x_j}^{x_{j+1}} \partial_t \eta(v(x, t)) \, dx \, dt + O(\Delta t)^3, \end{aligned}$$

where $\xi_1, \xi_2 \in (x_j, x_{j+1})$, and the error estimate for the midpoint rule has been used, namely,

$$E(f) = \int_a^b f(x) \, dx - (b-a) \left[f \left(\frac{a+b}{2} \right) \right] = f''(\xi) \frac{(b-a)^3}{24}, \quad \xi \in (a, b)$$

(see any text in numerical analysis—for example, [9]).

Let us consider now the contribution of the entropy fluxes. Again we describe the case in which $u'_j = (\bar{u}_j - \bar{u}_{j-1})/h$. Then the intermediate value of u is

$$u_j^{n+1/2} = \bar{u}_j^n - \frac{\lambda}{2} f'(\bar{u}_j^n) (\bar{u}_j^n - \bar{u}_{j-1}^n).$$

With manipulations very similar to the previous case, one finds that

$$\begin{aligned} \psi(u_j^{n+1/2}) &= \psi(v_j^{n+1/2}) \\ &+ \psi'(v_j^{n+1/2}) \left[-\frac{1}{2} (\Delta t)^2 \partial_x (f' \partial_x f)_j^n + \frac{1}{4} \lambda h^2 f'(v_j^n) (v_{xx})_j^n + \frac{h^2}{24} (v_{xx})_j^n \right] + O(\Delta t)^3. \end{aligned}$$

Thus, subtracting,

$$\psi(u_{j+1}^{n+1/2}) - \psi(u_j^{n+1/2}) = \psi(v_{j+1}^{n+1/2}) - \psi(v_j^{n+1/2}) + O(\Delta t)^3.$$

Applying the midpoint rule,

$$\begin{aligned} & \lambda \left[\psi(u_{j+1}^{n+1/2}) - \psi(u_j^{n+1/2}) \right] \\ &= \frac{1}{h} \int_{t^n}^{t^{n+1}} [\psi(v_{j+1}(t)) - \psi(v_j(t))] \, dt - \frac{(\Delta t)^3}{24h} [\psi_{tt}(x_{j+1}, \xi_1) - \psi_{tt}(x_j, \xi_2)] + O(\Delta t)^3, \end{aligned}$$

where $\xi_1, \xi_2 \in (t^n, t^{n+1})$. Thus

$$(3.14) \quad \lambda \left[\psi(u_{j+1}^{n+1/2}) - \psi(u_j^{n+1/2}) \right] = \frac{1}{h} \int_{t^n}^{t^{n+1}} \int_{x_j}^{x_{j+1}} \partial_x \psi(v(x, t)) \, dx \, dt + O(\Delta t)^3.$$

Finally, adding (3.13) and (3.14),

$$(3.15) \quad S_{j+1/2}^{n+1} = \frac{1}{\Delta t} \left\{ \frac{1}{h} \int_{t^n}^{t^{n+1}} \int_{x_j}^{x_{j+1}} (\partial_t \eta + \partial_x \psi) \, dx \, dt + O(\Delta t)^3 \right\}.$$

Since, for the exact smooth solution v , $\partial_t \eta + \partial_x \psi \equiv 0$, one gets $S_{j+1/2}^{n+1} = O(\Delta t)^2$.

Analogous results are found if other expressions are used for $(u')_j^n$, $(u')_{j+1}^n$, etc., except on local extrema, where the MinMod limiter chops the local extremum.

Let us now consider the case of a nonsmooth exact solution. We follow the argument described in [13]. In the nonsmooth case, the cell averages \bar{u}_j^n and $\bar{u}_{j+1/2}^{n+1}$ are at least bounded. Let

$$M^n = \max\{\bar{u}_j^n\}, \quad M^{n+1} = \max\{\bar{u}_{j+1/2}^{n+1}\}, \quad M^{n+1/2} = \max(M^n, M^{n+1}).$$

Substituting these bounds into (3.8), we find that

$$u^{n+1} \left(x_j + l \frac{h}{4} \right) < CM^{n+1/2}, \quad u^n \left(x_j + l \frac{h}{4} \right) < CM^{n+1/2},$$

where C is a constant, and $l = 1; 3$. Analogously, $u_j^{n+1/2} < \tilde{C}M^{n+1/2}$, where now \tilde{C} depends on f' . Using again the smoothness of η and ψ , we find

$$\begin{aligned} |S_{j+1/2}^{n+1}| &\leq \frac{1}{\Delta t} \left\{ \frac{1}{2} \left| \eta(u_{j+1/4}^{n+1}) \right| + \frac{1}{2} \left| \eta(u_{j+3/4}^{n+1}) \right| + \frac{1}{2} \left| \eta(u_{j+1/4}^n) \right| + \frac{1}{2} \left| \eta(u_{j+3/4}^n) \right| \right. \\ &\quad \left. + \lambda \left(\left| \psi(u_{j+1}^{n+1/2}) \right| + \left| \psi(u_j^{n+1/2}) \right| \right) \right\} \\ &\leq CM^{n+1/2} \frac{1}{\Delta t}. \quad \square \end{aligned}$$

Remark. The proof relies on the accuracy of the underlying numerical scheme, the accuracy of the space reconstruction, and the accuracy of the quadrature rules for the evaluation of the space and time integrals. Thus it is easy to extend the proof to higher-order schemes.

DEFINITION 2. Define the entropy production of CW3 and CW4 schemes on the control volume $V_{j+1/2}^{n+1} = [x_j, x_{j+1}] \times [t^n, t^{n+1}]$ by the expression

$$(3.16) \quad \begin{aligned} S_{j+1/2}^{n+1} &= \frac{1}{\Delta t} \left\{ \int_{x_j}^{x_{j+1/2}} \eta(u^{n+1}(x)) + \int_{x_{j+1/2}}^{x_{j+1}} \eta(u^{n+1}(x)) - \int_{x_j}^{x_{j+1/2}} \eta(u^n(x)) \right. \\ &\quad \left. - \int_{x_{j+1/2}}^{x_{j+1}} \eta(u^n(x)) + \lambda \left[\int_{t^n}^{t^{n+1}} \psi(u_{j+1}(t)) - \psi(u_j(t)) \right] \right\}. \end{aligned}$$

Here all integrals are computed with Simpson's rule. The values of u at the nodes of the quadrature rule for the space integrals are computed with the third order Compact Central WENO reconstruction for CW3 [21], and with the fourth order Central WENO reconstruction for CW4 [20]. The intermediate values of u required by the quadrature rule for the time integrals are computed with a third (fourth) order RK scheme, with natural continuous extension for CW3 (CW4, respectively).

We can now state the following corollary.

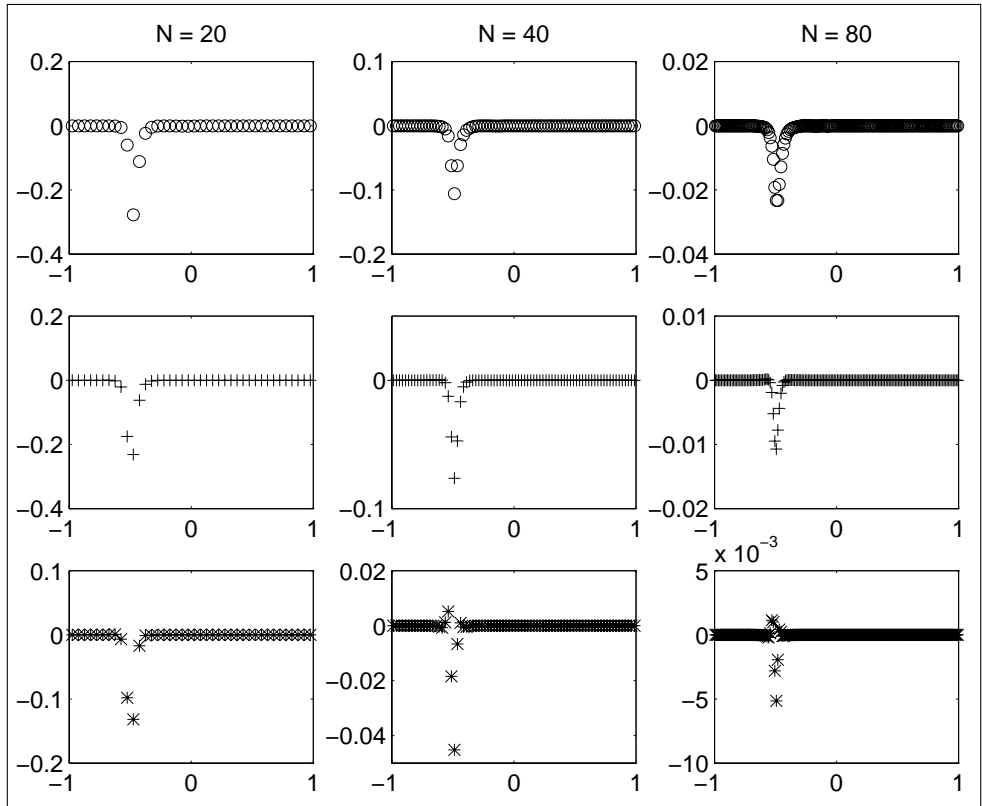


FIG. 4. Entropy production for NT, CW3, and CW4 schemes on a smooth flow. Burgers' equation, local entropy production at $T = 0.5$. From top to bottom: the NT scheme (o) with $\lambda = 0.33$, CW3 (+) with $\lambda = 0.66 * 3/7$, and CW4 (*) with $\lambda = 0.66 * 2/7$.

TABLE 1

Minimum entropy production on a smooth transition. Burgers' equation before shock formation at $T = 0.3$. The NT and Lax-Friedrichs schemes have $\lambda = 0.33$; the Godunov scheme has $\lambda = 0.66$; CW3 has $\lambda = 0.66 * 3/7$, and CW4 has $\lambda = 0.66 * 2/7$.

| | $N = 10$ | $N = 20$ | $N = 40$ | $N = 80$ | $N = 160$ | $N = 320$ |
|-----------------|----------|----------|----------|----------|-----------|-----------|
| Lax-Friedrichs | -.26292 | -.13834 | -.823E-1 | -.447E-1 | -.241E-1 | -.122E-1 |
| Godunov | -.18870 | -.10608 | -.624E-1 | -.340E-1 | -.183E-1 | -.928E-2 |
| Nessyahu-Tadmor | -.10097 | -.195E-1 | -.515E-2 | -.127E-2 | -.324E-3 | -.799E-4 |
| CW3 | -.922E-1 | -.996E-2 | -.106E-2 | -.135E-3 | -.176E-4 | -.222E-5 |
| CW4 | -.293E-1 | -.306E-2 | -.168E-3 | -.661E-5 | -.287E-6 | -.147E-7 |

TABLE 2

Rate of convergence for entropy production on a smooth transition. Burgers' equation before shock formation at $T = 0.3$. The NT and Lax-Friedrichs schemes have $\lambda = 0.33$; the Godunov scheme has $\lambda = 0.66$; CW3 has $\lambda = 0.66 * 3/7$, and CW4 has $\lambda = 0.66 * 2/7$.

| | $N = 10$ | $N = 20$ | $N = 40$ | $N = 80$ | $N = 160$ |
|-----------------|----------|----------|----------|----------|-----------|
| Lax-Friedrichs | 0.93 | 0.75 | 0.88 | 0.89 | 0.99 |
| Godunov | 0.83 | 0.77 | 0.88 | 0.89 | 0.98 |
| Nessyahu-Tadmor | 2.37 | 1.92 | 2.02 | 1.97 | 2.02 |
| CW3 | 3.21 | 3.23 | 2.97 | 2.94 | 2.99 |
| CW4 | 3.26 | 4.19 | 4.66 | 4.53 | 4.29 |

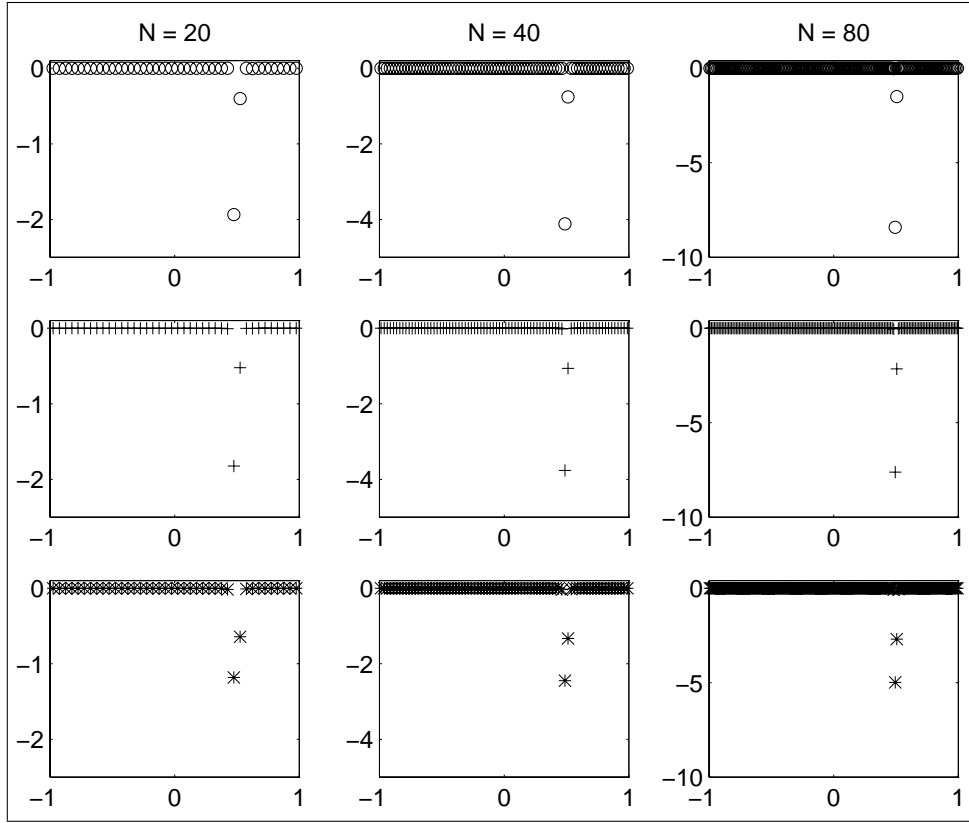


FIG. 5. Burgers' equation, local entropy production at $T = 1.5$. From top to bottom: the NT scheme (o) with $\lambda = 0.33$, CW3 (+) with $\lambda = 0.66 * 3/7$, and CW4 (*) with $\lambda = 0.66 * 2/7$.

TABLE 3

Minimum entropy production on a shock. Burgers' equation after shock formation at $T = 1.5$. The NT and Lax-Friedrichs schemes have $\lambda = 0.33$; the Godunov scheme has $\lambda = 0.66$; CW3 has $\lambda = 0.66 * 3/7$, and CW4 has $\lambda = 0.66 * 2/7$. The minima are always located on the shock.

| | $N = 10$ | $N = 20$ | $N = 40$ | $N = 80$ | $N = 160$ | $N = 320$ |
|----------------|----------|----------|----------|----------|-----------|-----------|
| Lax-Friedrichs | -0.4080 | -1.0429 | -2.2093 | -4.5666 | -9.2760 | -18.717 |
| Godunov | -0.4401 | -1.0337 | -2.1704 | -4.4568 | -9.0288 | -18.178 |
| NT | -0.7859 | -1.9356 | -4.1181 | -8.4142 | -17.049 | -34.357 |
| CW3 | -0.7795 | -1.8230 | -3.7608 | -7.6189 | -15.326 | -30.736 |
| CW4 | -0.5458 | -1.1817 | -2.4491 | -4.9821 | -10.046 | -20.167 |

COROLLARY 2. Consider the application of the CW3 and CW4 schemes for a single time step, starting from the exact cell averages, i.e., $\bar{u}_j^n = \bar{v}_j^n$. Consider a smooth entropy η and a smooth entropy flux ψ . Then the entropy production in the control volume $V_{j+1/2}^{n+1}$ satisfies the following estimates:

$$(3.17) \quad \begin{aligned} S_{j+1/2}^{n+1} &= O(\Delta t)^r \quad \text{on smooth flows,} \\ S_{j+1/2}^{n+1} &\leq O\left(\frac{1}{\Delta t}\right) \quad \text{on nonsmooth flows,} \end{aligned}$$

where $r = 3$ for CW3 and $r = 4$ for CW4.

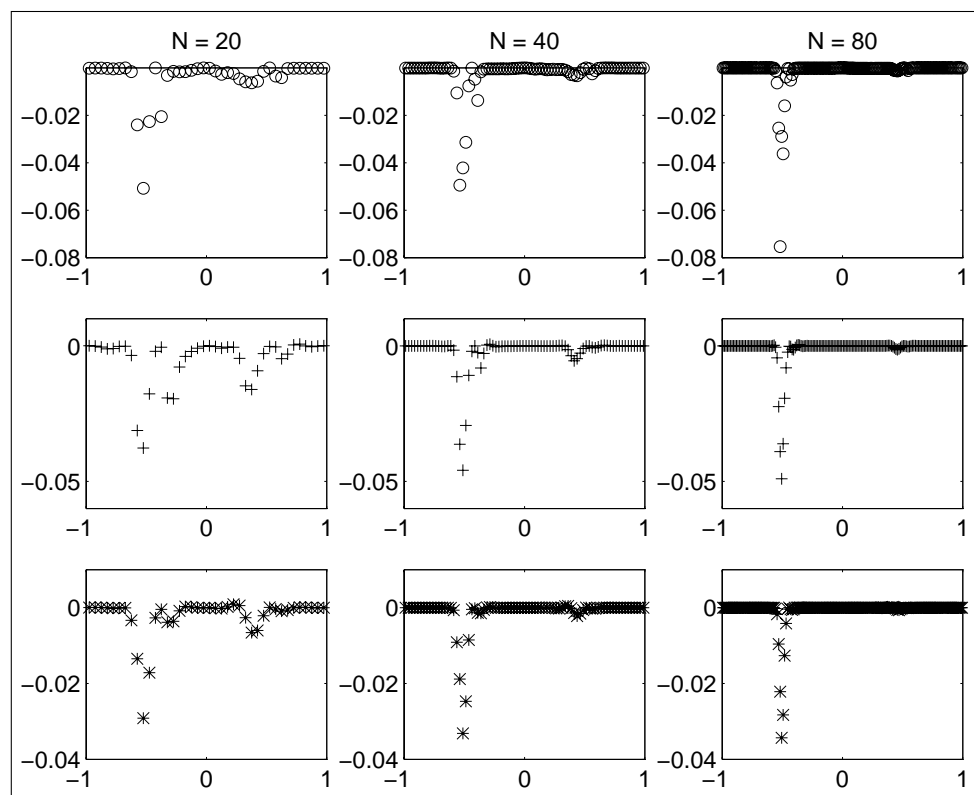


FIG. 6. Linear advection, local entropy production at $T = 1.5$. From top to bottom: the NT scheme (o) with $\lambda = 0.45$, CW3 (+) with $\lambda = 0.9 \cdot 3/7$, and CW4 (*) with $\lambda = 0.9 \cdot 2/7$.

Remark. Our numerical results on nonsmooth flows show that $S_{j+1/2} = O(1/\Delta t)$ on shocks, while $S_{j+1/2}$ is $O(1)$ on contacts (see Figures 9 and 8). Note that the exact entropy production in a cell crossed by a shock is indeed $O(1/\Delta t)$, at least in the scalar case (see (2.9)). On the other hand, the exact entropy production on a contact wave is zero, since, in this case, characteristics do not cross and the flow is reversible. These facts may explain the different rates we find experimentally. However, our estimates do not allow us to distinguish the two cases. Note also that the smoothness indicator proposed in [14] presents a behavior on contacts and shocks which is very similar to what we observe with entropy production.

3.3. Numerical results. Figures 4, 5, and 6 contain the plots of the density of entropy production obtained with the high-order schemes described in this section for Test #1 and Test #2. From top to bottom, we find the density of entropy production for the Nessyahu–Tadmor (NT) scheme, for the third order Compact Central WENO (CW3) scheme, and for the fourth order Central WENO (CW4) scheme.

The Nessyahu–Tadmor scheme has $\lambda = 0.5c$, where c is the Courant number of the flow, $c = 1/\max |f'(u)|$. The higher-order CW3 and CW4 have a stricter CFL restriction [4]: here we used $\lambda = c \cdot \frac{3}{7}$ for the CW3 scheme and $\lambda = c \cdot \frac{2}{7}$ for the CW4 scheme.

Figure 4 contains the plots of the entropy production obtained for the smooth flow of Test #1 at $T = 0.5$. Comparing it with Figure 1, we see that the qualitative

TABLE 4

Minimum entropy production on a contact discontinuity. Linear advection at $T = 1.5$. The NT and Lax–Friedrichs schemes have $\lambda = 0.45$; the Godunov scheme has $\lambda = 0.9$; CW3 has $\lambda = 0.9 \cdot 3/7$, and CW4 has $\lambda = 0.9 \cdot 2/7$. The minima are located in the cells containing the contact wave.

| | $N = 10$ | $N = 20$ | $N = 40$ | $N = 80$ | $N = 160$ | $N = 320$ |
|----------------|----------|----------|----------|----------|-----------|-----------|
| Lax–Friedrichs | -.04432 | -.04659 | -.05887 | -.07223 | -.08111 | -.08826 |
| Godunov | -.04359 | -.04818 | -.06036 | -.07324 | -.08186 | -.08878 |
| NT | -.03645 | -.05079 | -.04943 | -.07533 | -.09773 | -.11441 |
| CW3 | -.04685 | -.03765 | -.04590 | -.04901 | -.04725 | -.04413 |
| CW4 | -.02015 | -.02913 | -.03316 | -.03432 | -.03401 | -.03336 |

behavior of the entropy production is similar for all schemes studied in this work: in all cases entropy production is concentrated in the regions in which the solution is steepest, and spurious entropy production diminishes under grid refinement. However, for the high-order schemes, entropy production is much smaller, and it decreases much faster when the grid is refined than in the case of the first order schemes. We note that, for CW3 and for CW4, there are small positive overshoots in the entropy production, whose amplitude also decreases under grid refinement.

More quantitative data appear in Table 1, for Test #1 at $T = 0.3$. We chose the time $T = 0.3$ for the tables showing quantitative data for the smooth case, because at this time the solution of the initial value problem for Burgers' equation can be resolved as a smooth transition even by low-order schemes on coarse grids. Thus at this time the dependence of the entropy production on the grid mesh size is already very close to what its asymptotic behavior will be as $h \rightarrow 0$. The table shows the minima in entropy production as a function of the number of grid points per unit length, for all schemes studied here. These data clearly show that entropy production converges to zero, and at a faster rate for the high order schemes. The rate of convergence of the minima in the entropy production can be read from Table 2, where each entry contains the result of the expression $\log_2(\min(S_{j,h})/\min(S_{j,h/2}))$. Here it is readily seen that the minima in entropy production go to zero with approximately the same order of accuracy as that of the scheme.

Figure 5 shows the entropy production obtained for Test #1 at $T = 1.5$. The solution now contains a shock, and the peak in entropy production is located on the shock. As in the case of the first order schemes (see Figure 2) the entropy production on the shock doubles as the mesh parameter h is halved. Quantitative data can be found in Table 3. The presence of these large peaks and their behavior under grid refinement can be used to single out shocks from the rest of the flow (see section 4.1).

Finally, in Figure 6 we show the entropy production for the linear advection problem of Test #2, at $T = 1.5$. Comparing this with Figure 3, we see that the entropy production has a peak for all schemes, corresponding to the position of the contact discontinuity, and a smaller peak corresponding to the angular point. The amplitude of the peak on the angular point decreases under grid refinement, but at a slower rate than in the case of the smooth flow of Test #1. For the higher-order schemes, the amplitude of the peak on the contact discontinuity is approximately constant under grid refinement. The actual amplitude of the peak on the contact discontinuity as a function of the number of grid points appears in Table 4.

It is interesting to compare the powers in the rate of convergence of the entropy production on a smooth flow ($O(h^r)$) and on a shock ($O(h^{-1})$) with the rates given by the indicator proposed in [13] that are, respectively, $O(h^{r+3})$ and $O(h^2)$. The difference in the rate of convergence for smooth flows and shocks is $O(h^{r+1})$ in both

cases. It is worthwhile to note that the entropy indicator involves only the time levels n and $n + 1$, and it can be applied straightforwardly to a high-order scheme, such as CW4.

4. Applications. In this section we study some applications of the study of the local entropy production.

We study the possibility of using the entropy production as a discontinuity detector in section 4.1 and as an error indicator in section 4.2. Finally in section 4.3 we show the results obtained with a simple adaptive strategy, which uses entropy production as an indicator, with the aim of increasing the resolution of the numerical scheme.

4.1. Entropy production as a discontinuity detector. We study the data in the density of entropy production on different transitions to see whether it is possible to use the entropy production to automatically classify discontinuities. This information can be applied in several ways.

It is important in a strategy of grid adaptivity to select the regions where a shock occurs to prevent the crowding of too many grid points close to the discontinuity. High-order schemes are in fact able to resolve well a shock wave even on a coarse grid.

It can also be useful to be able to select the regions containing contact discontinuities. These transitions are in fact poorly resolved even by high-order schemes. Algorithms acting as slope correctors are available to improve the resolution of contact discontinuities, such as the artificial compression method of [29]. These slope correctors typically artificially increase the slope of characteristics, transforming contact waves into shocks. They are not entropic, so it is advisable to apply them only on discontinuities, to prevent the occurrence of expansion shocks.

We have already seen in the previous section that entropy production can be used as a discontinuity detector. In fact we have shown that entropy production is bounded by $O(\frac{1}{h})$ terms on shocks, while it is $O(h^r)$ on smooth transitions. Moreover the data in Table 4 indicate that entropy production is approximately $O(1)$ on contact discontinuities.

We now extend these results to the case of systems of equations, showing the behavior of the entropy production on three Riemann problems from gas dynamics. The results show that the behavior observed in the scalar case carries over to the case of systems of equations. Next we will consider two test problems with wave interactions.

For systems of equations, the entropy inequality can be written provided that there exists an entropy pair $\eta(u)$ and $\psi(u)$ such that η is a convex function and the entropy flux ψ satisfies the compatibility condition

$$\nabla^T \eta(u) Jf(u) = \nabla^T \psi(u),$$

where Jf is the Jacobian of f (see [10]). We consider a polytropic ideal gas. Here, u is the vector of conserved variables, $u = (\rho, \rho v, E)^T$, where ρ is the density, v is the gas velocity, and E is the total energy per unit volume; $E = \rho e + \frac{1}{2} \rho v^2$ and e is the internal energy per unit mass. The flux is

$$f(u) = \begin{pmatrix} \rho v \\ \rho v^2 + p \\ v(E + p) \end{pmatrix}, \quad p = \rho e(\gamma - 1),$$

where p is the pressure and $\gamma = 1.4$ is the specific heats ratio for air.

The thermodynamic entropy is $s = s_0 + C_V \log(\frac{e}{\rho^{\gamma-1}})$, where C_V is the specific heat at constant volume, and s_0 is an arbitrary constant. The quantity that satisfies the entropy inequality is the entropy per unit volume, namely, $\eta(u) = -\rho s(u)$, with entropy flux $\psi(u) = -v\eta(u)$ (see [10]). In this work, we will take

$$(4.1) \quad \eta(u) = -\rho \log\left(\frac{e}{\rho^{\gamma-1}}\right).$$

In fact, the constant C_V appearing in the thermodynamic entropy enters the expression of the entropy production as a multiplicative constant, and therefore it does not alter the behavior of entropy production with respect to h . Moreover, it is easy to prove that entropy production, as it has been defined in this work, does not depend on s_0 , so one can choose $s_0 = 0$ with no loss of generality.

We start with three Riemann problems, where the data are chosen in order to issue a simple wave solution. Here L and R denote the left and right states, respectively.

Single left moving rarefaction wave.

$$\begin{pmatrix} \rho \\ v \\ p \end{pmatrix}_L = \begin{pmatrix} 1.02222 \\ -0.6179 \\ 1 \end{pmatrix} \quad \begin{pmatrix} \rho \\ v \\ p \end{pmatrix}_R = \begin{pmatrix} \rho^* \\ v^* \\ 0.4 \end{pmatrix},$$

with $\rho^* = \rho_L * (p_R/p_L)^{(1/\gamma)}$, $v^* = v_L + 2/(\gamma-1)(a_R - a_L)$, and $a = \sqrt{(\gamma p/\rho)}$ being the speed of sound. The initial discontinuity was placed in $x_0 = 0.8$.

Single right moving contact discontinuity.

$$\begin{pmatrix} \rho \\ v \\ p \end{pmatrix}_L = \begin{pmatrix} 1 \\ 1 \\ 1 \end{pmatrix} \quad \begin{pmatrix} \rho \\ v \\ p \end{pmatrix}_R = \begin{pmatrix} 0.4 \\ 1 \\ 1 \end{pmatrix}.$$

Here the initial discontinuity is placed at $x_0 = 0.2$.

Single right moving shock wave.

$$\begin{pmatrix} \rho \\ v \\ p \end{pmatrix}_L = \begin{pmatrix} 1 \\ 0.8276 \\ 1 \end{pmatrix} \quad \begin{pmatrix} \rho \\ v \\ p \end{pmatrix}_R = \begin{pmatrix} 0.5313 \\ 0.1 \\ 0.4 \end{pmatrix}.$$

Again the initial discontinuity is placed at $x_0 = 0.2$.

In all three cases the computation is stopped at $T = 0.4$, and free flow boundary conditions are enforced. Note that all jumps in the initial data have approximately the same strength.

The scalar schemes described above have been applied to the system of gas-dynamic equations componentwise. In the Nessyahu–Tadmor scheme, the intermediate value of the unknown $u^{n+1/2}$ was predicted using the Jacobian of the flux function. In the CW3 and CW4 schemes, we used global smoothness indicators (see [20]), so that all components of the solution have the same smoothness indicator, and the scheme can be applied componentwise.

Figure 7 shows the density of entropy production obtained on a single rarefaction wave for all central schemes considered in this work. Note that the vertical scale is different for all plots in this figure. We see that the entropy production decreases fast under grid refinement for all schemes. For the Lax–Friedrichs scheme, entropy production decreases roughly as $O(h)$ as in the scalar case. The higher-order schemes

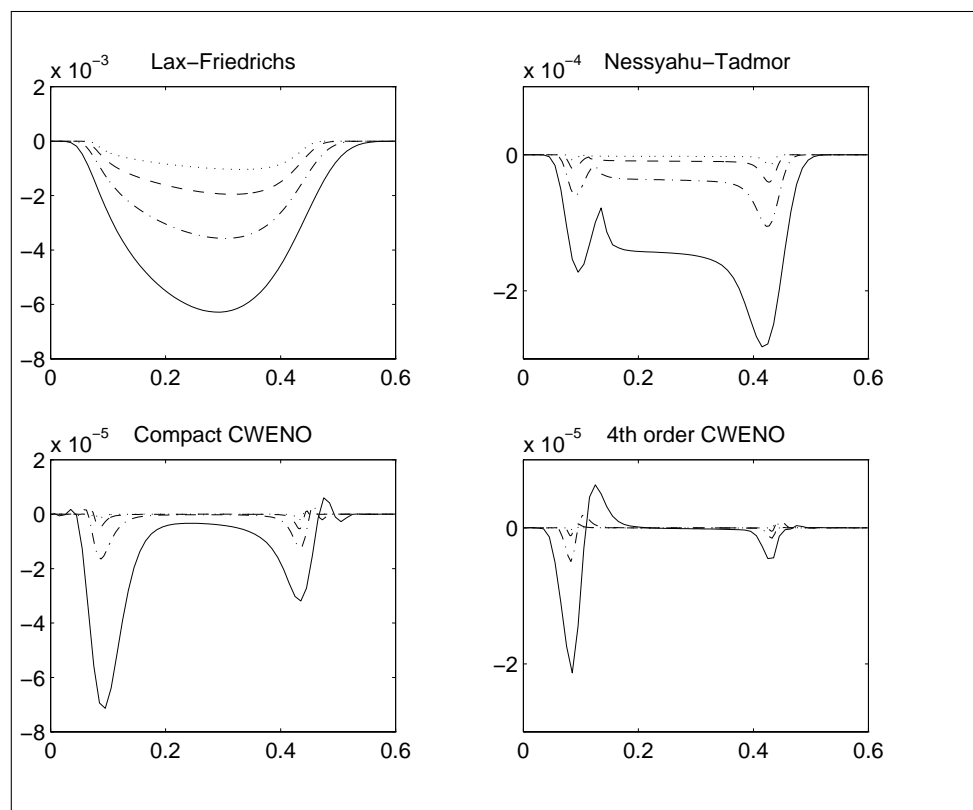


FIG. 7. Entropy production on a single rarefaction wave. Comparison of the entropy production of Lax-Friedrichs, Nessyahu-Tadmor, CW3, and CW4 schemes with several grid sizes. The solid line corresponds to $N = 100$, the dashed-dotted line to $N = 200$, the dashed line to $N = 400$, and the dotted line to $N = 800$. The Courant number for this problem is roughly $c = 0.56$. The Lax-Friedrichs and Nessyahu-Tadmor schemes have $\lambda = 0.25$. CW3 has $\lambda = \frac{3}{7}c$ and CW4 has $\lambda = \frac{2}{7}c$.

detect the irregularity in the solution due to the head and tail of the rarefaction wave. Here the rate of decay of the entropy production is slower, but away from these regions of nonsmoothness, we again see that the entropy production converges to zero faster for the higher order schemes.

We also note that the third and fourth order schemes produce overshoots of positive entropy production, whose amplitude goes to zero fast under grid refinement.

In Figure 8, we can find the results obtained on the single contact wave. It appears that for all schemes tested the entropy production in this case is approximately constant under grid refinement, with the lower-order schemes producing more spurious numerical entropy than the higher-order schemes.

Finally, Figure 9 contains the results obtained for a single shock. We immediately see that on shocks the entropy approximately doubles as the mesh width is halved for all schemes studied. Moreover, the number of grid points on which the shock is spread is independent of h . Therefore the total entropy dissipated on the shock

$$\mathcal{S} = \sum_j S_j h \rightarrow \text{const} \quad \text{as } h \rightarrow 0,$$

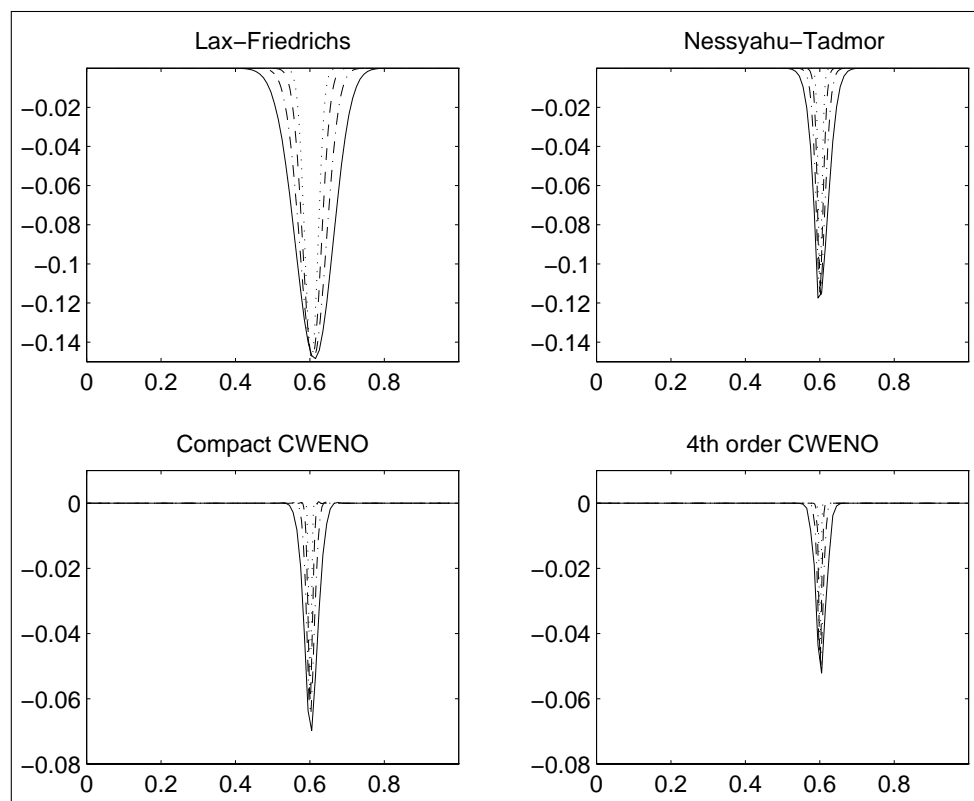


FIG. 8. Entropy production on a single contact discontinuity. Comparison of the entropy production of Lax-Friedrichs, Nessyahu-Tadmor, CW3, and CW4 schemes with several grid sizes. The solid line corresponds to $N = 100$, the dashed-dotted line to $N = 200$, the dashed line to $N = 400$, and the dotted line to $N = 800$. The Courant number for this problem is roughly $c = 0.35$. The Lax-Friedrichs and Nessyahu-Tadmor schemes have $\lambda = 0.5c$. CW3 has $\lambda = \frac{3}{7}c$ and CW4 has $\lambda = \frac{2}{7}c$.

where the sum is extended to the cells on which the shock is spread.

Comparing Tables 1 and 3 and the figures above, we clearly see that the local entropy production on the smooth transition is orders of magnitude smaller (in absolute value) than the entropy dissipated on the shock, especially on fine grids and for the higher-order schemes. Moreover, from Figure 9, we note that the cells containing the shock are characterized by very sharp and isolated peaks in entropy production. Therefore shocks seem to be easily identified.

The next two test problems show that it is possible to track shocks with entropy production. Namely, we plot the space-time position of those cells for which

$$|S_{j+1/2}^n| \geq Kh^\alpha.$$

We start with a simple scalar problem of wave interaction for Burgers' equation. The initial data is:

$$u(x, t = 0) = 2 - \sin(\pi x) + \sin(2\pi x), \quad \text{on } [-1, 1],$$

with periodic boundary conditions. The exact solution develops two shock waves at $t \simeq 0.15$, which collide in $t \simeq 0.62$, resulting in a single shock. Figure 10 shows the

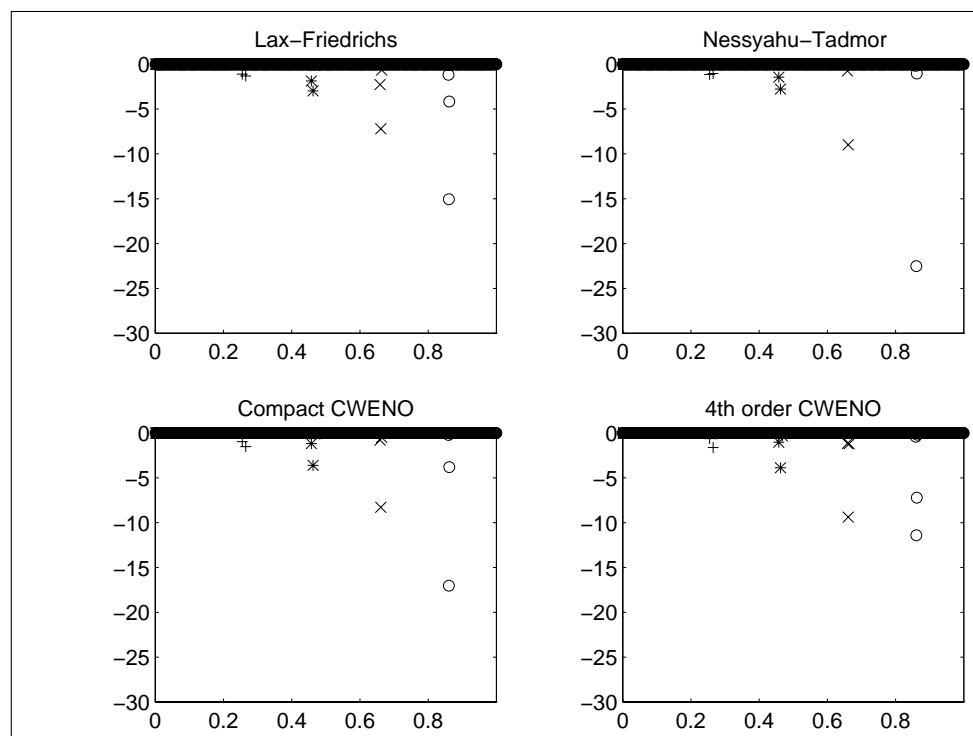


FIG. 9. Entropy production on a single shock wave. Comparison of the entropy production of Lax–Friedrichs, Nessyahu–Tadmor, CW3, and CW4 schemes with several grid sizes. In these plots the shock waves have been shifted in order to show them more clearly. The “+” corresponds to $N = 100$, “*” to $N = 200$, “x” to $N = 400$, and “o” to $N = 800$. The Courant number for this problem is roughly $c = 0.49$. The Lax–Friedrichs and Nessyahu–Tadmor schemes have $\lambda = 0.25$. CW3 has $\lambda = \frac{3}{7}c$ and CW4 has $\lambda = \frac{2}{7}c$.

results obtained with the Nessyahu–Tadmor scheme and with CW4 for $K = 1$ and $\alpha = 0$.

The location of the two shocks is clearly visible and well resolved. Also, the shock formation time and the instant of collision are well represented.

The second test problem is the Woodward and Colella blast wave problem [30]. The initial data contain two Riemann problems: $u(x, t = 0) = u_L$ for $0 \leq x < 0.1$, $u(x, t = 0) = u_C$ for $0.1 \leq x \leq 0.9$, and $u(x, t = 0) = u_R$ for $0.9 < x \leq 1$, where $\rho \equiv 1$, $\rho v \equiv 0$, $p_L = 1000$, $p_C = 0.01$, and $p_R = 100$. The computational domain is $[0, 1]$, with reflective boundary conditions.

The effects of the complex wave interactions of this test problem on the shock trajectories can be seen in Figure 11.

Both plots were obtained by the CW4 scheme with 1600 grid points. In both cases, we chose a normalization factor for K to take account of the fact that the magnitude of the numerical solution varies by orders of magnitude during its evolution, namely, $K = \|\eta(u(\cdot, t^n))\|_\infty$. Thus, in this case, K depends on t^n . On the left $\alpha = 0$, while on the right $\alpha = 1/2$.

Each of the two initial Riemann problems originates a strong shock wave traveling toward the interior of the domain, a strong rarefaction speeding toward the wall, and a contact discontinuity that follows the shock. Shortly, the left rarefaction issued

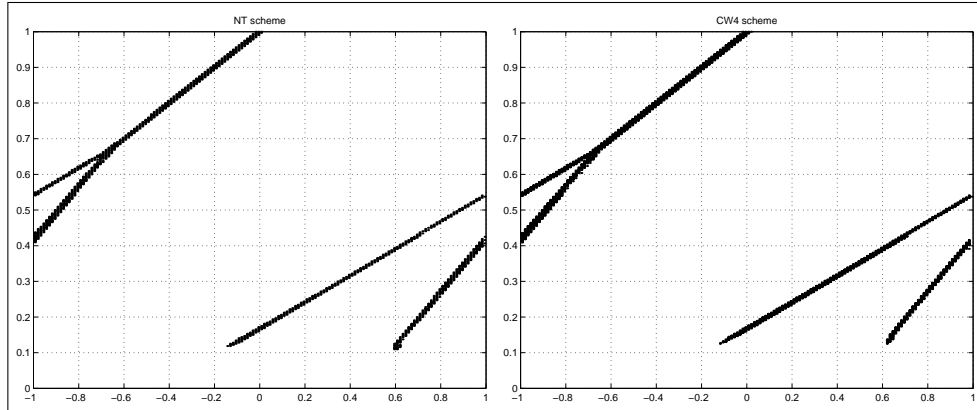


FIG. 10. Shock tracking on a scalar equation. $N = 160$. Left: NT scheme. Right: CW4.

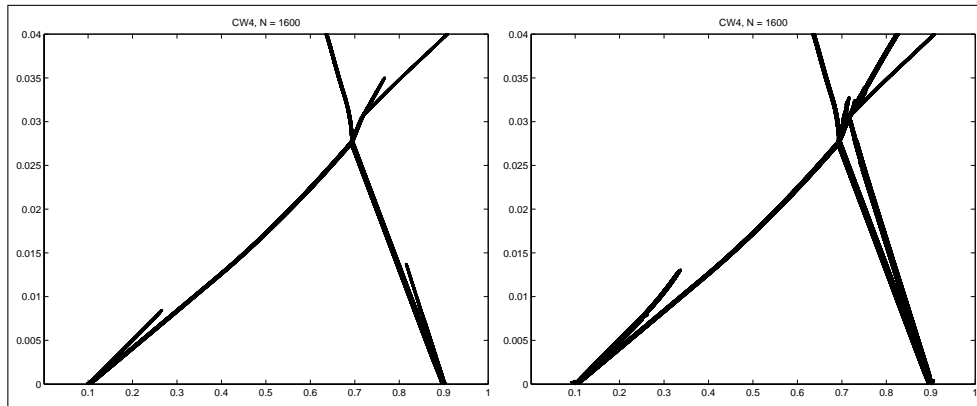


FIG. 11. Shock tracking in gas dynamics. $N = 1600$. Left: Tracking cells with $|S_j| > \|\eta\|_\infty h^0$. Right: Tracking cells with $|S_j| > \|\eta\|_\infty h^{1/2}$.

by the initial data bounces back from the reflective wall and interacts with the left contact wave eroding its strength and slowing it down. Although Figure 11 does not show the trajectory of the rarefaction waves, the track of shocks and of the initial stages of the contact waves motion can be detected.

The collision of the two initial shocks generates two shocks and a contact wave. A short time later, the right shock further interacts with the initial right contact, while the left shock interacts with a reflected rarefaction, slowing down. These details are also visible in Figure 11, especially for $\alpha = 1/2$, which allows us to see the complete trajectory of the right contact.

For both values of α , the trajectory of shock waves is clearly shown, together with the speed variations due to the shocks' interactions with other waves. Also visible are the initial stages of the trajectory of strong contacts: as these are spread by numerical diffusion, they disappear from Figure 11.

As α is increased (right plot), more waves are tracked, i.e., the right contact wave and the contact wave resulting from the shock collision. These results can be compared with the density contours for this problem (see Figure 1 of [30]) that are in close agreement with Figure 11, except for the left contact wave, which is in fact

TABLE 5

Maximum and minimum entropy production on a smooth transition. Burgers' equation, $T = 0.5$, $\lambda = 0.66 * 3/7$ for CW3, $\lambda = 0.66 * 2/7$ for CW4.

| | CW3 | | CW4 | |
|---------|---------|---------|---------|---------|
| | min | max | min | max |
| N = 10 | -.61582 | .155e-3 | -.44818 | .381e-4 |
| N = 20 | -.23138 | .938e-4 | -.13171 | .963e-3 |
| N = 40 | -.07630 | .224e-3 | -.04519 | .521e-2 |
| N = 80 | -.01071 | .158e-3 | -.00514 | .114e-2 |
| N = 160 | -.00158 | .710e-4 | -.28e-3 | .114e-3 |
| N = 320 | -.20e-3 | .185e-4 | -.11e-4 | .707e-5 |

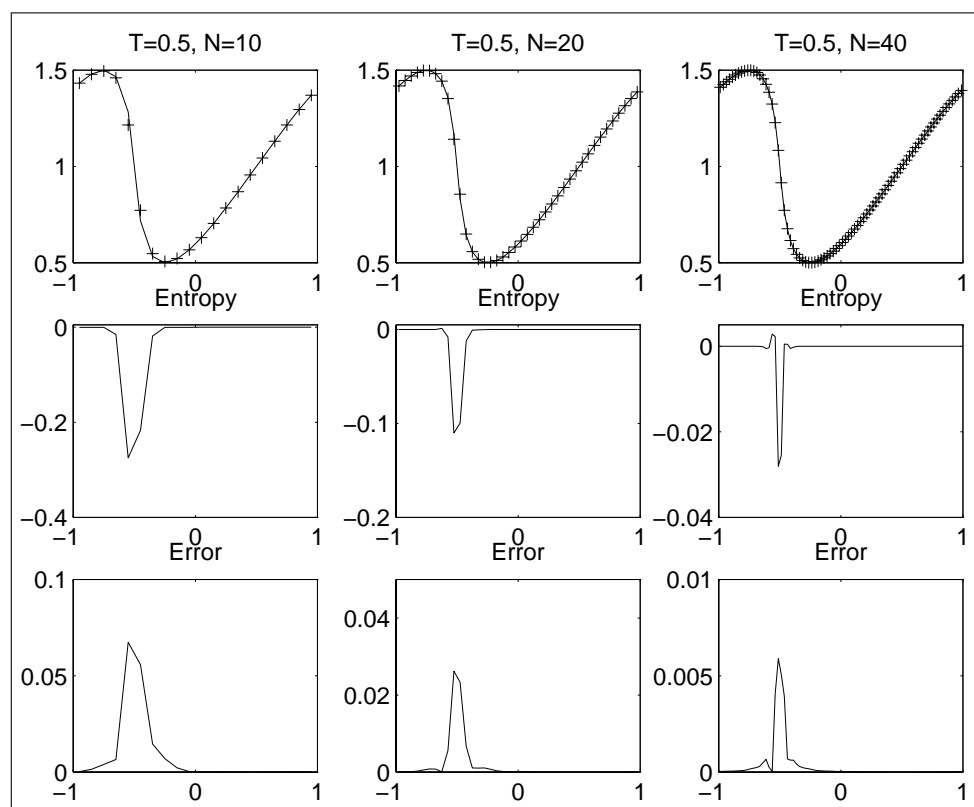


FIG. 12. Burgers' equation. Solution at $T = 0.5$. Entropy production for the CW4 scheme (second row) and error (third row) on a smooth wave, with $\lambda = 0.66 * 2/7$.

poorly resolved by all central schemes studied here.

More results on systems of equations can be found in [23].

We end this section by discussing the behavior of the positive overshoots in entropy production for the CW3 and CW4 schemes. There are no results on the entropic properties of high order schemes (third and higher order). Figure 7 clearly shows that there are positive overshoots in the entropy production for the CW3 and CW4 schemes. The same behavior can be seen in Figure 4. The amplitude of these overshoots goes to zero fast under grid refinement, as can be seen in Table 5. These schemes therefore may not be entropic. However, these data suggest that CW3 and

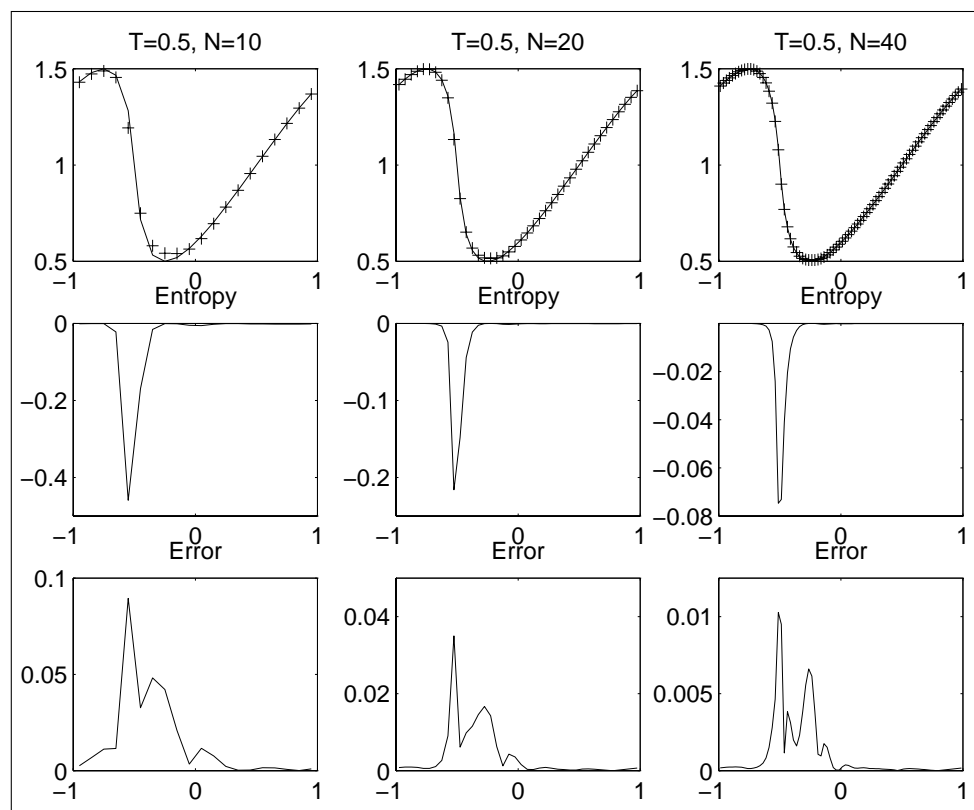


FIG. 13. Burgers' equation. Solution at $T = 0.5$. Entropy production for the Nessyahu–Tadmor scheme (second row) and error (third row) on a smooth wave, with $\lambda = 0.33$.

CW4 might be essentially entropic, in the sense that positive overshoots in the entropy production are possible, but their amplitude goes to zero under grid refinement.

4.2. Entropy production as error indicator. We have seen that the spurious entropy production on smooth flows goes to zero with the same rate of local truncation error.

To compare the local behavior of the error and the entropy production, we consider again Test #1 at $T = 0.5$.

Figure 12 shows a comparison between the actual error (third row) and the entropy production (second row) for the CW4 scheme on Burgers' equation, before shock formation. We see that entropy production indeed peaks where the error is largest, and both quantities have a similar behavior. Moreover the amplitude and width of the peaks in the error and in the entropy production undergo the same changes under grid refinement.

In Figure 13, the same test problem has been applied to the Nessyahu–Tadmor scheme, with the MinMod limiter. Here we note that the error has two main contributions: where the transition is steep, the error is due to a lack of resolution in the grid. This phenomenon is also caught by the entropy production, which has a peak in this region. Another source of error is the clipping phenomenon characteristic of the MinMod limiter in the presence of local extrema. This phenomenon is responsible for the secondary peaks that appear in the plots of the error. This source of error

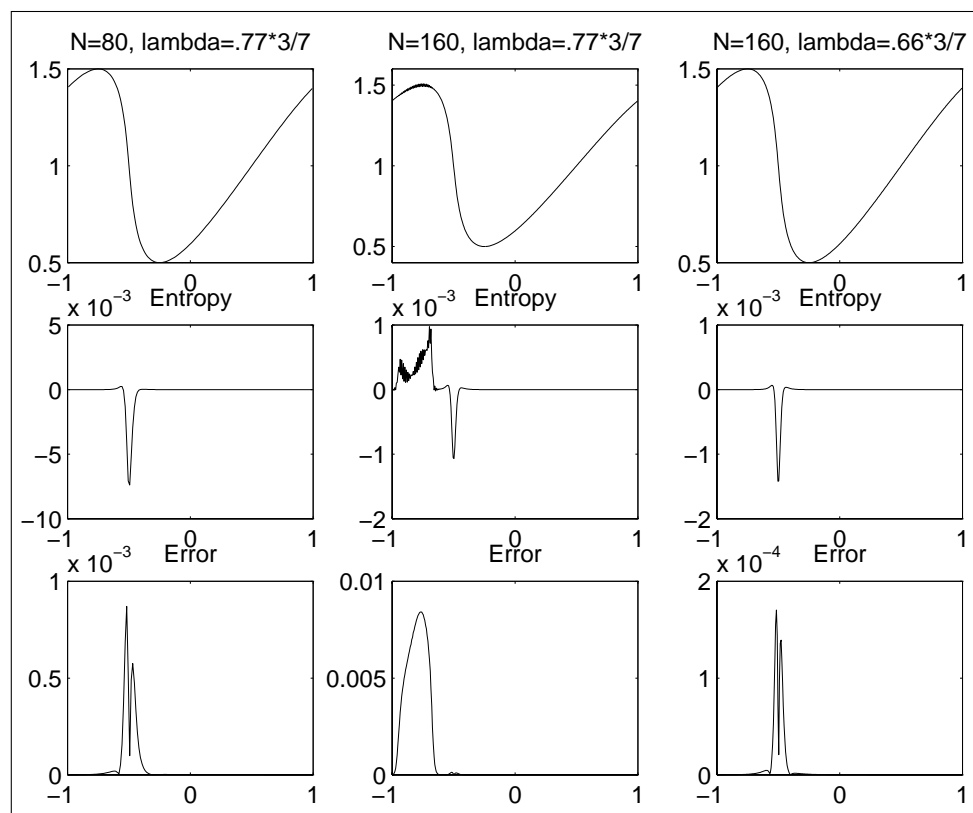


FIG. 14. Burgers' equation. Solution at $T = 0.5$. Entropy production for the third order CW3 scheme (second row) and error (third row) on a smooth wave.

unfortunately is not detected by the entropy production. The entropy production in fact is very small in regions where the numerical solution is approximately constant, and therefore is not able to detect this type of error. Moreover the estimate of section 3.2 for the rate of convergence does not hold on local extrema. Note that even error indicators based on the local derivatives of the numerical solution would not detect the need for grid refinement in these regions.

Another example is shown in Figure 14. The test problem is the same as before, i.e., Burgers' equation before shock formation, with the third order CW3 scheme. In the first two columns, we have $\lambda = 0.77 * 3/7$. This is slightly above the actual CFL for this scheme, which, for this problem, is $\lambda = 0.66 * 3/7$. For $N = 80$ (left column) the solution is stable, and both the entropy and the error have a similar behavior. In the second column, with $N = 160$, the numerical solution is slightly unstable. Small wiggles appear in the maximum of the solution, although they are barely visible on this scale. These of course are reflected in the error, which however is still small. Interestingly, the entropy reacts to these unphysical oscillations with a region of positive entropy production that not only signals that the error is larger here than in the neighboring cells but also shows that something is wrong in the numerical solution.

As λ is decreased (third column), the wiggles disappear, together with the region of positive entropy production.

Therefore the magnitude of the density of entropy production mimics the behavior of the error, and in this sense, it can be used as an a posteriori indicator for grid, or scheme, adaptivity.

Moreover, we can also use the sign of the entropy production to signal the need for more dissipation. We can achieve this goal by decreasing the mesh ratio λ or by switching to a lower order scheme.

4.3. Scheme adaption. In this section we use the entropy production as an indicator of the need to locally modify the scheme in order to increase resolution. This strategy was proposed in [14], with a different indicator.

High resolution schemes are nonlinear in order to prevent the development of spurious oscillations close to discontinuities in the solution. The nonlinearity of the schemes tested in this work occurs in the space reconstruction, either through slope limiting (as in the Nessyahu–Tadmor scheme) or with a proper bias towards smooth stencils (in CW3 and CW4). Although these algorithms are effective in the prevention of spurious oscillations, it is well known that they introduce some numerical diffusion. Thus it is advisable to use nonlinear reconstructions only where they are really needed, with an adaptive strategy.

In particular, we use entropy production to pick those cells in which it is necessary to apply a nonlinear reconstruction. The modified scheme becomes

$$(4.2) \quad \begin{cases} \text{If } |S_{j+1/2}^n| > Kh^\alpha & \text{apply a nonlinear reconstruction,} \\ \text{else} & \text{apply a linear reconstruction.} \end{cases}$$

When $|S_{j+1/2}^n|$ is large, we assume there is some “structure” in the control volume $[x_j - h/2, x_j + h/2] \times [t^{n-1}, t^n]$. Then we must allow for the possibility that this wave will escape to the neighboring cells in the following time step. Thus, when $|S_{j+1/2}^n|$ is large, we modify the scheme in the three cells $j-1, j, j+1$.

We test this idea on the gas-dynamics problem described in [14]. The problem consists of a Mach 3 shock interacting with an acoustic wave. The initial condition is $u = u_L$ for $x \leq 0$, and $u = u_R$ for $x > 0$. The computational domain we used is $[-6, 10]$, with free-flow boundary conditions. The left (L) and right (R) states are given by

$$\begin{pmatrix} \rho \\ v \\ p \end{pmatrix}_L = \begin{pmatrix} 3.857143 \\ -0.920279 \\ 10.3333 \end{pmatrix}, \quad \begin{pmatrix} \rho \\ v \\ p \end{pmatrix}_R = \begin{pmatrix} 1 + 0.2 \sin(5x) \\ -3.549648 \\ 1 \end{pmatrix}.$$

The reciprocal of the maximum characteristic speed for this flow is $c \simeq 0.219$; thus we pick $\lambda = 0.2\lambda_0$, where $\lambda_0 = 0.5$ for the Nessyahu–Tadmor scheme, $\lambda_0 = 3/7$ for CW3 and $\lambda_0 = 4/7$ for CW4. The solution is printed at $T = 2$. The figures show the density component of the solution on the interval $[-6, 4]$.

We consider two cases:

- (a) $\alpha = 0$: in this case only strong shocks are detected. The results depend weakly on the constant K . In the tests shown in the figures, $K = 1$.
- (b) $\alpha = 1$: now weak shocks can also be detected, but the results are more sensitive to the choice of K . A similar sensitivity can also be observed in the results shown in [14] on this test problem.

We first show the results obtained with the Nessyahu–Tadmor scheme and with the CW3 and CW4 schemes, with $\alpha = 0$ and $K = 1$. The results appear in Figure 15, 16, and 17, respectively. The dashed curve is a reference solution, obtained with

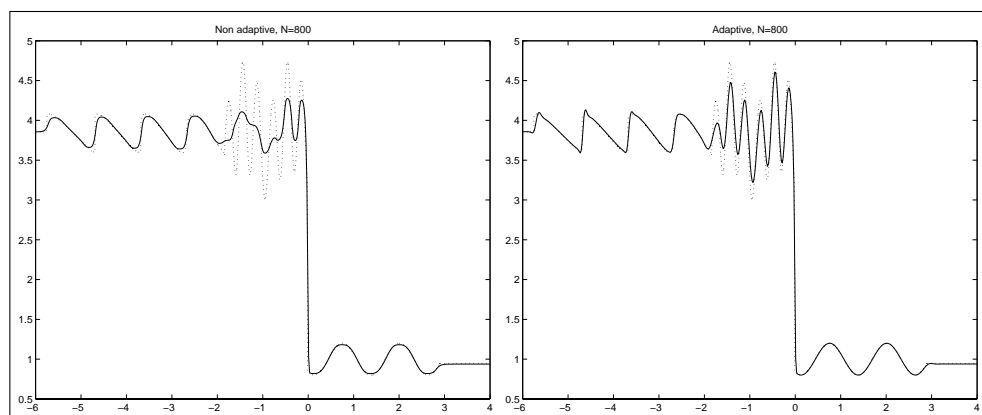


FIG. 15. NT scheme, density. On the right, the reconstruction is nonlinear only close to the strong shock.

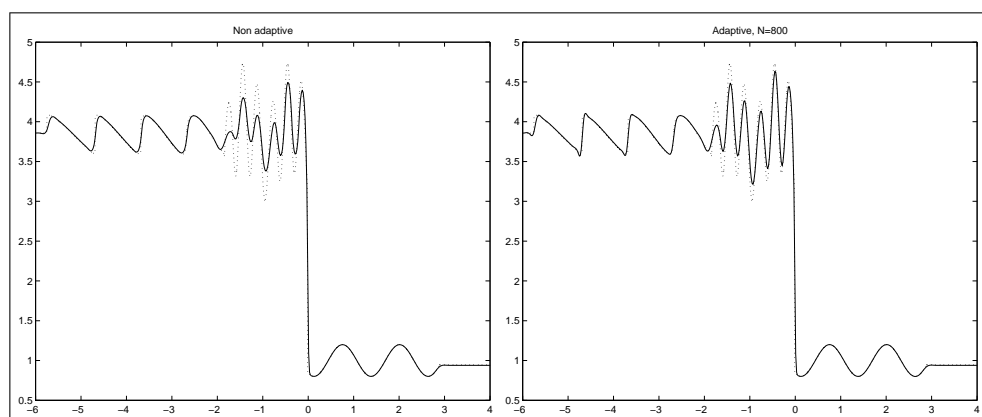


FIG. 16. CW3 scheme, density. On the right, the reconstruction is nonlinear only close to the strong shock.

CW4 and 12800 grid points. In all three cases, the nonlinear reconstruction is applied only in three or four cells around the strong shock. This is enough to prevent the appearance of a deep undershoot at the location of the strong shock.

The improvement in resolution for the Nessyahu–Tadmor scheme is indeed striking. In the cells where the linear scheme is applied, the slopes of the numerical solution are evaluated with simple central differences. However, small irregularities appear behind the weak shocks of the adaptive scheme.

For CW3 and CW4, the nonlinear scheme employs the Central WENO reconstruction, as in [21] and [20]. The linear scheme of the adaptive strategy is based on Central WENO reconstruction with linear weights: in this case the local polynomials that are combined to yield the reconstruction are weighted with the optimal accuracy constants, with no need to compute the smoothness indicators.

In the CW3 and CW4 schemes, the increase in resolution obtained with the adaptive strategy is apparent, but it is not as striking as with the Nessyahu–Tadmor scheme. This is due to the fact that these schemes do not degenerate to first order close to discontinuities, maintaining high resolution in the presence of shocks. On the

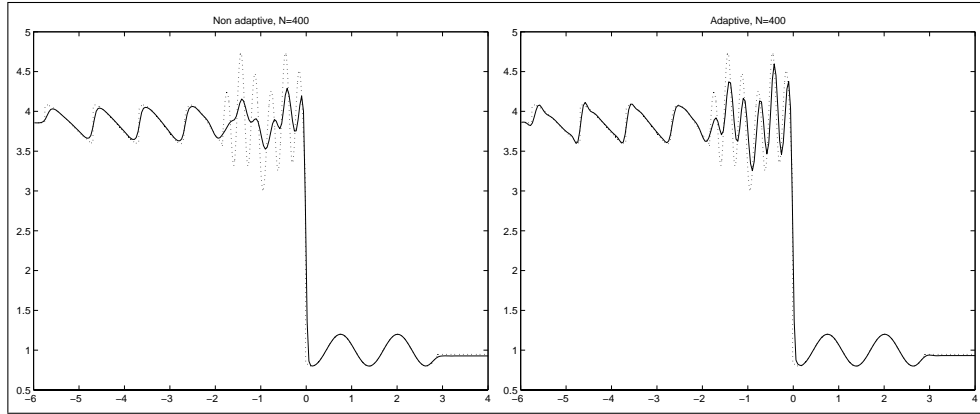


FIG. 17. CW4 scheme, density. On the right, the reconstruction is nonlinear only close to the strong shock. In this figure, $N = 400$.

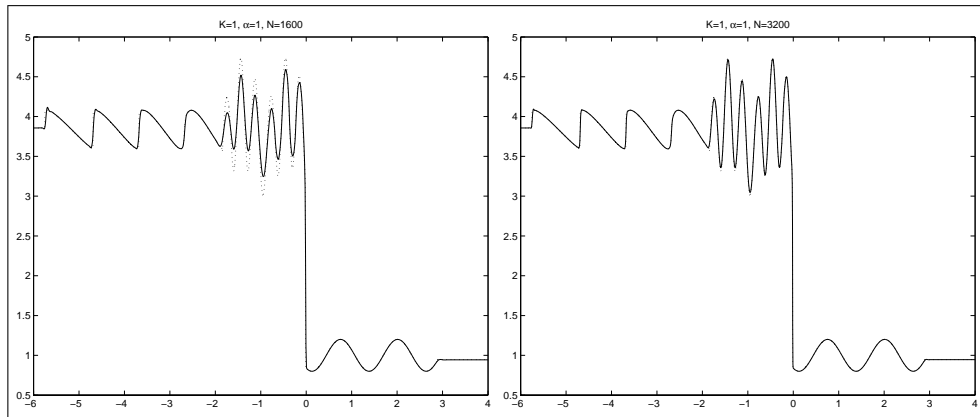


FIG. 18. Nessyahu–Tadmor scheme, density: The threshold of the adaptive scheme has $\alpha = 1$ and $K = 1$.

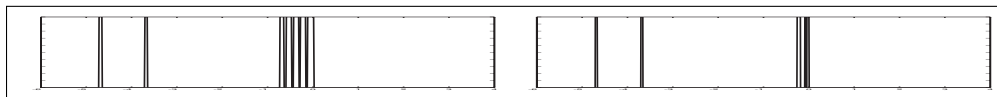


FIG. 19. Nessyahu–Tadmor scheme: Cells in which the nonlinear reconstruction is applied, with $\alpha = 1$ and $K = 1$. Left: $N = 1600$; right: $N = 3200$.

other hand, spurious small wiggles appear on the weak shocks. Overall, the adaptive scheme yields a higher resolution than the scheme with nonlinear reconstruction in each cell.

If $\alpha = 1$, the threshold of the adaptive scheme can include also weak shocks, and, if the grid is fine enough, weak shocks are singled out from smooth transitions. We illustrate this on the Nessyahu–Tadmor scheme.

Figure 18 contains the results given by the Nessyahu–Tadmor scheme with $\alpha = 1$ and $K = 1$, with two grid sizes. Figure 19 shows the cells selected by the adaptive strategy for the application of the nonlinear reconstruction for both grids.

The adaptive strategy gives a higher resolution than the nonadaptive nonlinear

scheme. Since, in this case, weak shocks are also labelled by the adaptive scheme, the spurious wiggles that were noticed before have disappeared. Note also that with grid refinement the number of cells behind the strong shock, labelled for the nonlinear reconstruction, has decreased.

Remark. Further work on this topic will be based on the extension of the computation of the local entropy production to schemes based on nonstaggered grids. The proof of Proposition 1 still holds if the entropy flux ψ is replaced by a smooth numerical entropy flux Ψ , consistent with the exact entropy flux ψ . This makes it possible to extend the definition of entropy production to schemes based on nonstaggered grids, for which the numerical solution u is not defined at the walls $x = x_j \pm h/2$ of the control volumes.

Acknowledgments. I wish to thank Denise Aregba Driollet, Roberto Natalini, and Giovanni Russo for several helpful discussions.

REFERENCES

- [1] J. G. ANDREWS AND K. W. MORTON, *A posteriori error estimation based on discrepancies in an entropy variable*, Int. J. Comput. Fluid Dyn., 10 (1998), pp. 183–198.
- [2] M. J. BERGER, *Local adaptive mesh refinement for shock hydrodynamics*, J. Comput. Phys., 82 (1989), pp. 64–84.
- [3] M. J. BERGER AND R. LEVEQUE, *Adaptive mesh refinement using wave-propagation algorithms for hyperbolic systems*, SIAM J. Numer. Anal., 35 (1998), pp. 2298–2316.
- [4] F. BIANCO, G. PUPPO, AND G. RUSSO, *High order central schemes for hyperbolic systems of conservation laws*, in Hyperbolic Problems: Theory, Numerics, Applications, Vol. I, Internat. Ser. Numer. Math. 129, Birkhäuser-Verlag, 1999, pp. 55–64.
- [5] F. BOUCHUT, CH. BOURDARIAS, AND E. B. PERTHAME, *A MUSCL method satisfying all the numerical entropy inequalities*, Math. Comp., 65 (1996), pp. 1439–1461.
- [6] B. COCKBURN, *A Simple Introduction to Error Estimation for Nonlinear Hyperbolic Conservation Laws*, Lecture Notes. Available online at <http://www.math.umn.edu/~cockburn>.
- [7] B. COCKBURN, G. KARNIADAKIS, AND C.-W. SHU, *The development of discontinuous Galerkin methods*, in Discontinuous Galerkin Methods: Theory, Computation and Applications, Lect. Notes Comput. Sci. Eng. 11, B. Cockburn, G. Karniadakis, and C.-W. Shu, eds., Springer-Verlag, Berlin, 2000, pp. 3–50.
- [8] B. COCKBURN AND C.-W. SHU, *TVB Runge–Kutta local projection discontinuous Galerkin finite element method for conservation laws II: General framework*, Math. Comp., 52 (1989), pp. 411–435.
- [9] V. COMINCIOLI, *Analisi numerica: Metodi, modelli, applicazioni*, McGraw-Hill, Milan, 1990.
- [10] E. GODLEWSKI AND P.-A. RAVIART, *Numerical Approximation of Hyperbolic Systems of Conservation Laws*, Springer-Verlag, New York, 1996.
- [11] A. HARTEN, B. ENGQUIST, S. OSHER, AND S. CHAKRAVARTHY, *Uniformly high order accurate essentially non-oscillatory schemes III*, J. Comput. Phys., 71 (1987), pp. 231–303.
- [12] G.-S. JIANG AND C.-W. SHU, *Efficient implementation of weighted ENO schemes*, J. Comput. Phys., 126 (1996), pp. 202–228.
- [13] S. KARNI AND A. KURGANOV, *Local error analysis for approximate solutions of hyperbolic conservation laws*, Numer. Math., submitted.
- [14] S. KARNI, A. KURGANOV, AND G. PETROVA, *A smoothness indicator for adaptive algorithms for hyperbolic systems*, J. Comput. Phys., 178 (2002), pp. 323–341.
- [15] D. KRÖNER AND M. OHLBERGER, *A posteriori error estimates for upwind finite volume schemes for nonlinear conservation laws in multidimensions*, Math. Comp., 69 (2000), pp. 25–39.
- [16] S. N. KRUKOV, *First order quasilinear equations in several independent variables*, Math. USSR Sb., 10 (1970), pp. 217–243.
- [17] A. KURGANOV, S. NOELLE, AND G. PETROVA, *Semidiscrete central-upwind schemes for hyperbolic conservation laws and Hamilton–Jacobi equations*, SIAM J. Sci. Comput., 23 (2001), pp. 707–740.
- [18] M. KÜTHER, *Error estimates for the staggered Lax–Friedrichs scheme on unstructured grids*, SIAM J. Numer. Anal., 39 (2001), pp. 1269–1301.
- [19] R. J. LEVEQUE, *Numerical Methods for Conservation Laws*, Lectures Math. ETH Zürich, Birkhäuser-Verlag, Basel, 1992.

- [20] D. LEVY, G. PUPPO, AND G. RUSSO, *Central WENO schemes for hyperbolic systems of conservation laws*, Math. Model. Numer. Anal., 33 (1999), pp. 547–571.
- [21] D. LEVY, G. PUPPO, AND G. RUSSO, *Compact central WENO schemes for multidimensional conservation laws*, SIAM J. Sci. Comput., 22 (2000), pp. 656–672.
- [22] H. NESSYAHU AND E. TADMOR, *Non-oscillatory central differencing for hyperbolic conservation laws*, J. Comput. Phys., 87 (1990), pp. 408–463.
- [23] G. PUPPO, *Numerical entropy production on shocks and smooth transitions*, J. Sci. Comput., 17 (2002), pp. 263–271.
- [24] J. QIU AND C.-W. SHU, *On the construction, comparison, and local characteristic decomposition for high order central WENO schemes*, J. Comput. Phys., 183 (2002), pp. 187–209.
- [25] C.-W. SHU AND S. OSHER, *Efficient implementation of essentially non-oscillatory shock capturing schemes*, J. Comput. Phys., 77 (1988), pp. 439–471.
- [26] C.-W. SHU, *Essentially non-oscillatory and weighted essentially non-oscillatory schemes for hyperbolic conservation laws*, in Advanced Numerical Approximation of Nonlinear Hyperbolic Equations, Lecture Notes in Math. 1697, A. Quarteroni, ed., Springer-Verlag, Berlin, 1998, pp. 325–432.
- [27] T. SONAR AND E. SÜLI, *A dual graph norm refinement indicator for finite volume approximations of the Euler equations*, Numer. Math., 78 (1998), pp. 619–658.
- [28] E. TADMOR, *Approximate solutions of nonlinear conservation laws*, in Advanced Numerical Approximation of Nonlinear Hyperbolic Equations, Lecture Notes in Math. 1697, A. Quarteroni, ed., Springer-Verlag, Berlin, 1998, pp. 1–149.
- [29] H. YANG, *An artificial compression method for ENO schemes, the slope modification method*, J. Comput. Phys., 89 (1990), pp. 125–160.
- [30] P. WOODWARD AND P. COLELLA, *The numerical simulation of two-dimensional fluid flow with strong shocks*, J. Comput. Phys., 54 (1984), pp. 115–173.
- [31] M. ZENNARO, *Natural continuous extensions of Runge–Kutta methods*, Math. Comp., 46 (1986), pp. 119–133.